

A pole to pole west Pacific atmospheric teleconnection during August

Keith M. Hines¹ and David H. Bromwich^{1,2}

Received 25 September 2001; revised 26 February 2002; accepted 12 April 2002; published 27 September 2002.

[1] An observational analysis is presented that reveals an August teleconnection involving both the Northern Hemisphere (NH) and the Southern Hemisphere (SH). The teleconnection includes three primary anomalies in the monthly average surface pressure field: (1) a high southern latitude component including Wilkes Land, Antarctica, the nearby Southern Ocean, and the Ross Sea, (2) a SH midlatitude component near Australia and New Zealand, and (3) a NH subtropical component over the extreme western Pacific Ocean. Surface pressure for the SH high-latitude anomaly is negatively correlated to the other two primary anomalies. The SH midlatitude and NH subtropical component are positively correlated. Furthermore, the teleconnection is correlated to surface pressure near the Aleutian Islands. The teleconnection anomalies result from tropical convection on intraseasonal timescales. Monsoon rainfall over East Asia during August is correlated to the teleconnection. Furthermore, August precipitation at several other locations in the NH and SH is modulated by the teleconnection. Two different sets of numerical experiments with the National Center for Atmospheric Research (NCAR) Community Climate Model version 2 (CCM2) show a similar-appearing teleconnection during late boreal summer. The modeled teleconnection, however, is forced from high southern latitudes.

INDEX TERMS: 3309 Meteorology and Atmospheric Dynamics: Climatology (1620); 3349 Meteorology and Atmospheric Dynamics: Polar meteorology; 3354 Meteorology and Atmospheric Dynamics: Precipitation (1854); 3374 Meteorology and Atmospheric Dynamics: Tropical meteorology; 9355 Information Related to Geographic Region: Pacific Ocean

Citation: Hines, K. M., and D. H. Bromwich, A pole to pole west Pacific atmospheric teleconnection during August, *J. Geophys. Res.*, 107(D18), 4359, doi:10.1029/2001JD001335, 2002.

1. Introduction

[2] Observational and modeling studies reveal teleconnections during late boreal summer with high-latitude, midlatitude, and low-latitude components of both the Northern Hemisphere (NH) and Southern Hemisphere (SH). One of the best known teleconnections between the tropics and extratropics is the correlation between warm events of the El Niño-Southern Oscillation (ENSO) and the Pacific North America (PNA) pattern especially during boreal winter [e.g., Horel and Wallace, 1981; Trenberth *et al.*, 1998]. Teleconnections are also found between the polar regions and tropical sea surface temperature and pressure variations of ENSO [e.g., Smith and Stearns, 1993; Gloersen, 1995; Simmonds and Jacka, 1995; Cullather *et al.*, 1996; Bromwich *et al.*, 2000].

[3] While ENSO plays a key role in global variations on the interannual timescale, the primary component of the tropical climate variability on the shorter intraseasonal timescale is the Madden-Julian oscillation (MJO) [Madden and

Julian, 1971, 1994]. The MJO is denoted by tropical convection anomalies typically on a zonal scale of wave numbers 1–3 [e.g., Krishnamurti *et al.*, 1985; Salby and Hendon, 1994; Waliser *et al.*, 1999]. We shall use the term intraseasonal oscillations (ISOs) to describe phenomena, including the MJO, on a timescale of about 2 weeks to 2 months.

[4] Connections between the tropical ISO and extratropical climate are less well known than linkages of ENSO to midlatitude and polar climate. Extensive work, however, has been done on the role of the ISO within tropical climatology, the Asian monsoon and the Australian summer monsoon [e.g., Davidson *et al.*, 1983; Lau *et al.*, 1988; Wang and Rui, 1990; Joseph *et al.*, 1991; Vincent *et al.*, 1991; Lau and Yang, 1996; Wang and Xie, 1998]. There is a strong intraseasonal modulation of the summer monsoon precipitation over China [e.g., Samel *et al.*, 1999]. Furthermore, many studies show that subtropical cyclones and anticyclones are linked to intraseasonal changes in the tropical convection and velocity [e.g., Weickmann *et al.*, 1985; Kiladis and Weickmann, 1992; Lau *et al.*, 1994; Wang and Xu, 1997; Kiladis and Mo, 1998; Maloney and Hartmann, 1998].

[5] Fewer studies detail the connection of the tropical ISO to regions poleward of the Asian and Australian monsoons and subtropical vortices. The review paper by Madden and Julian [1994] discusses previous work on midlatitude connections to the tropical ISO and notes that robust responses are not easily found in the midlatitudes. Nevertheless, studies

¹Polar Meteorology Group, Byrd Polar Research Center, The Ohio State University, Columbus, Ohio, USA.

²Atmospheric Sciences Program, Department of Geography, The Ohio State University, Columbus, Ohio, USA.

do show that the circulation associated with the tropical ISO extends poleward of the subtropics [e.g., *Hendon and Salby*, 1994; *Lau et al.*, 1994; *Kiladis and Mo*, 1998; *Mo and Higgins*, 1998]. Recently, *Mo and Higgins* [1998] find that the tropical ISO can induce the Pacific–South America pattern in the SH extratropics during austral winter.

[6] Here we present observational and modeling evidence that significant teleconnections are found during late austral winter (boreal summer) with impacts from the SH high latitudes to the tropical ISO and the East Asian monsoon. The work was motivated by teleconnections between high southern latitudes and the East Asian monsoon found in previous numerical modeling studies by *Bromwich et al.* [1998a, 1998b] examining the impacts of Antarctic sea ice removal. With the National Center for Atmospheric Research (NCAR) Community Climate Model version 2 (CCM2), they show that removing Antarctic sea ice results in a chain of anomalies in the West Pacific sector that extend to the region of the East Asian monsoon. Simulated changes in the monsoon circulation produce a statistically significant increase in September large-scale precipitation over northern China and a corresponding decrease over central China [*Bromwich et al.*, 1998a].

[7] The current study ties anomalies of surface pressure near Antarctica with the split jet stream in the Australian/South Pacific sector as well as with the tropical circulation and East Asian monsoon precipitation. Section 2 describes the data sets and station observations for this study. Section 3 shows the global structure of the teleconnection. The results of the NCAR CCM2 simulations are discussed in section 4. The time evolution of the teleconnection anomalies on intraseasonal timescales is demonstrated in section 5. The conclusions are presented in section 6.

2. Data Sources

[8] The primary data source is monthly mean fields from the National Centers for Environmental Prediction (NCEP)/NCAR Reanalysis [*Kalnay et al.*, 1996; *Kistler et al.*, 2001]. From the NCEP/NCAR Reanalysis, 24 years of monthly averaged surface pressure data from 1977 to 2000 are taken. The initial year is selected due to spurious changes in the reanalysis fields over Asia prior to 1977 [*Hines et al.*, 2000]. There are also spurious negative trends in reanalysis surface pressure for high southern latitudes. The effect of the latter is minimized by removing the linear regression trend at every grid point south of 40°S.

[9] Individual station observations have been used to support findings with the reanalysis fields. Monthly station observations are obtained from several sources. Jo Jacka of the Antarctic Cooperative Research Center has provided monthly average surface pressure and surface temperature up to the early 1990s at multiple high southern latitude stations. This has been supplemented by surface pressure and temperature observations at Antarctic stations Casey, Dumont d'Urville and Mawson for 1960–1996 supplied by Brad Murphy and Paul Pettré of Centre National de Recherches Meteorologiques and at Scott Base 1957–1996 supplied by the Antarctic Meteorology Research Center at the University of Wisconsin-Madison.

[10] For correlation studies, monthly surface pressure observations at various locations up to the year 1999 are

also obtained from the Global Historical Climatology Network [*Vose et al.*, 1992] and the National Climatic Data Center. Selected stations include 39 stations over Australia south of 20°S, 3 stations from eastern China east of 120°E, 8 stations in southern Japan between 24°N and 33°N, and 5 stations in southwestern Alaska near the Aleutian Islands.

[11] Monthly precipitation data are taken from the 2.5° latitude by 2.5° longitude Xie and Arkin precipitation data set [*Xie and Arkin*, 1997] for 1979–2000. The data are from merged precipitation fields including input from rain gauges, 5 kinds of satellite estimates and numerical model predictions.

3. Observations of the Teleconnection

3.1. Primary Anomaly Pattern

[12] The teleconnection patterns in the West Pacific sector can be seen in monthly mean fields for August from the NCEP/NCAR Reanalysis. Figure 1 shows the 1977–2000 correlation of monthly averaged surface pressure during August to that over southeastern Australia at 37.5°S, 142.5°E. The point at 37.5°S, 142.5°E is chosen as the reference point due to the relatively large magnitude of the correlations for distant points. Similar patterns can be found with the choice of different reference points. According to Figure 1, when the reanalysis pressure over southeast Australia is above average, the pressure will tend to be below average to the south over Wilkes Land, Antarctica and to the southeast over the Ross Sea. During such Augusts, the pressure will also tend to be above average in a subtropical NH region centered near 25°N, 130°E. The magnitude of the correlations exceeds 0.75 for locations over Wilkes Land in high southern latitudes and over the subtropical western Pacific in the NH.

[13] The Student's t-test can be used to gain an indication of the statistical significance of the major features in Figure 1. If the 24 Augusts represent a random sample, then the number of degrees of freedom for the t-test would be 22. Due to autocorrelation between years, however, the effective degrees of freedom are reduced [*Bretherton et al.*, 1999]. The hatched areas in Figures 1 and 2 are significant at the 95% confidence level adjusted for autocorrelation. The features over Wilkes Land to the south and the subtropical NH to the north easily meet the criteria for statistical significance.

[14] While Figure 1 shows the correlation between points, Figure 2 gives an indication of the actual amplitude of the surface pressure anomalies for the teleconnection. The five selected Augusts, 1982, 1987, 1994, 1995, and 1998, with above average pressure at the point 40°S, 145°E over southeastern Australia are averaged and compared to that of the five selected Augusts, 1981, 1984, 1990, 1991, and 1992, with below average surface pressure at the same point. This point is slightly closer to a pressure anomaly maximum than the reference point for Figure 1. The surface pressure difference between the averages is displayed globally in Figure 2. Hatching again shows where the anomalies are statistically significant at 95% confidence according to the Student's t-test. The pressure difference can be very large. Over the South Pacific near 40°S, 160°E, the difference between the composites exceeds 13 hPa. To the south near Antarctica, surface pressure is negatively correlated to Australia in Figure 1. Therefore, the difference in Figure 2 is negative there and can exceed 12 hPa at 70°S in Wilkes Land. There is

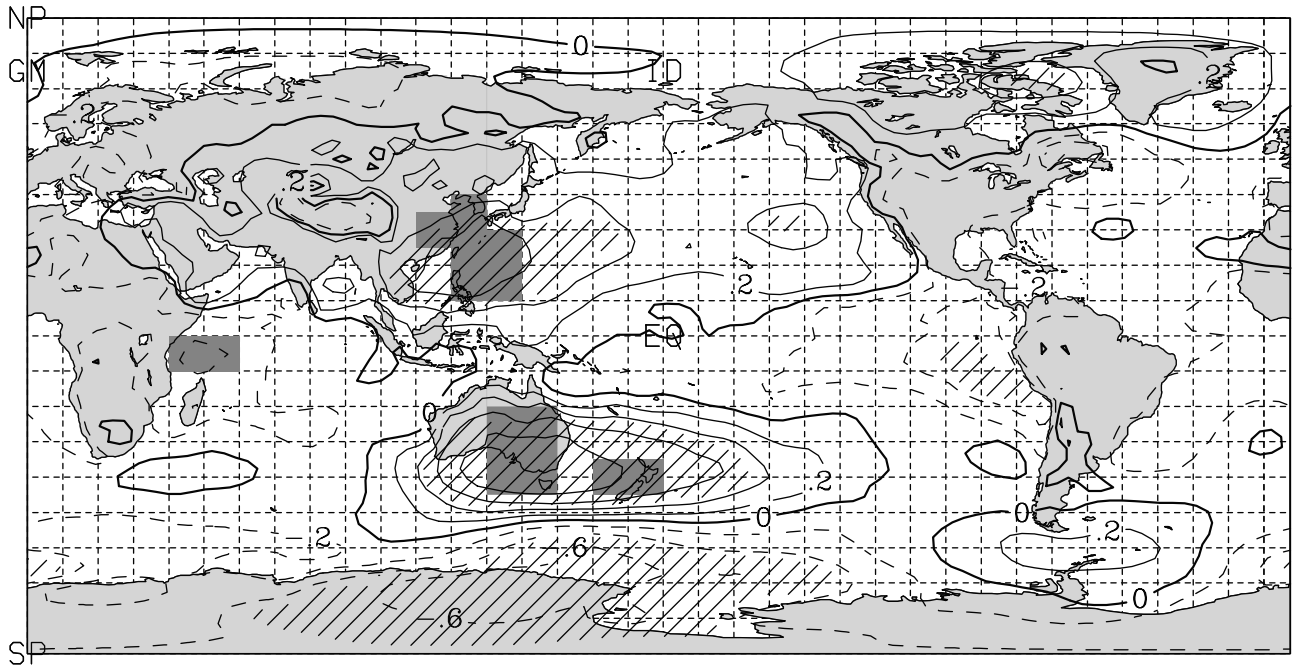


Figure 1. Correlation of surface pressure to that of 37.5°S, 142.5°E for monthly average Augusts of the NCEP/NCAR Reanalysis during 1977–2000. Contour interval is 0.2. Dashed contours show negative values. Heavy shaded areas are precipitation regions 1–6 (see text for details). Continents are light shaded. Hatched areas are significant at the 95% confidence level. Grid spacing is 10°, and the convergence of 180° longitude and the Equator is marked EQ.

also a second minimum of similar magnitude centered near 65°S, 150°W to the east of the Ross Sea. At 25°N, 130°E in the vicinity of the southwest Pacific high in the subtropical NH, the difference is positive with a maximum value about 5 hPa. While this magnitude is less than that of the extrema

of the SH, the pressure near the high is very important in determining the location and intensity of the summer monsoon rain front over East Asia [e.g., Lau and Li, 1984].

[15] Figure 2 also indicates that the pressure is increased near the Aleutian Islands in high northern latitudes during

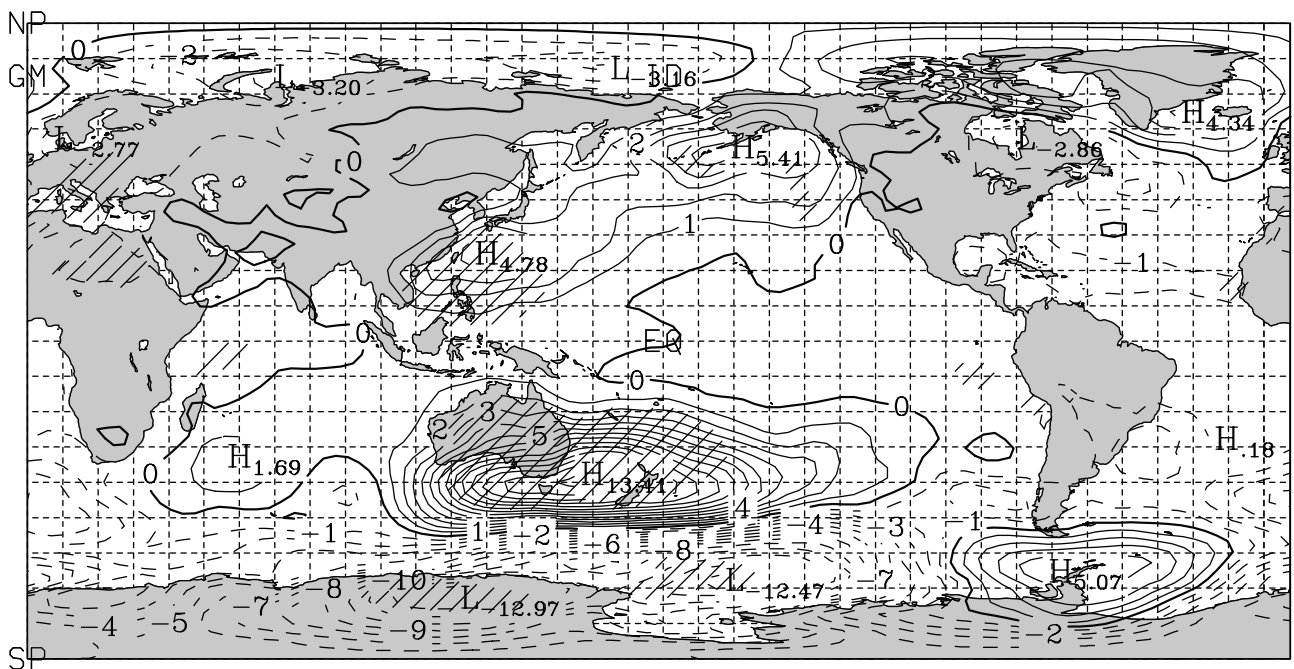


Figure 2. Map of difference in average August surface pressure (hPa) of the NCEP/NCAR Reanalysis between 5 selected months of above average pressure and 5 selected months of below average surface pressure at 40°S, 145°E. Contour interval is 1 hPa. Thick contour is 0.

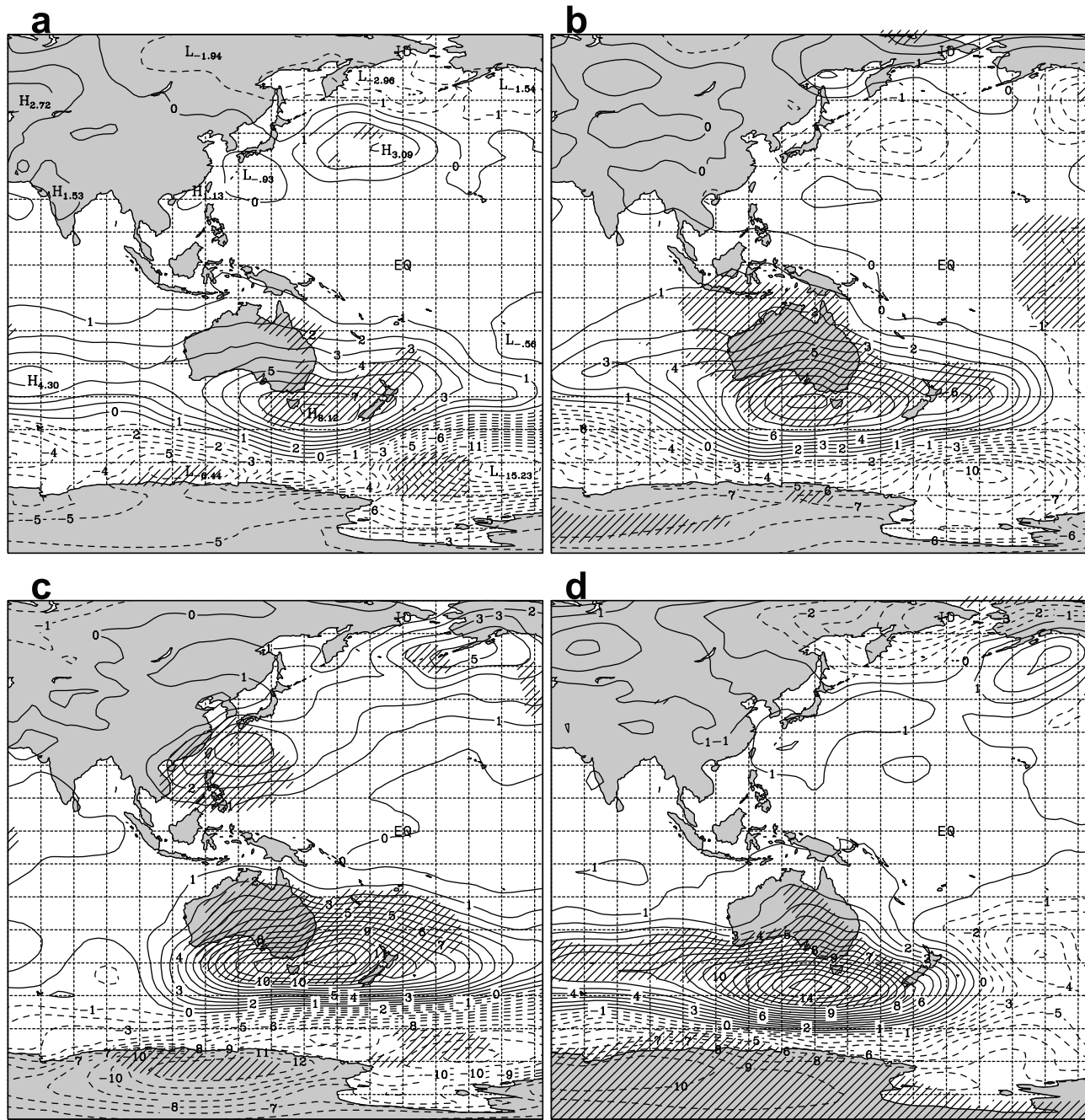


Figure 3. Same as Figure 2, except for (a) June, (b) July, (c) August, and (d) September.

Augusts when the pressure is increased over Australia. This feature, however, is not clearly seen in Figure 1. Figure 2 implies that the impacts of the August teleconnection extend from high southern latitudes to high northern latitudes.

[16] Key components of the atmospheric variability in the Pacific sector are linked through the pattern in Figures 1 and 2. The point-to-point correlation pattern in Figure 1 highlights locations where the interannual variability is very large in the SH. The variance of surface pressure is large near the location of the circumpolar trough surrounding Antarctica [Thompson and Wallace, 2000]. Furthermore, the large gradient in pressure in Figure 2 south of Australia and New Zealand is near the location of the southern branch of

the split jet stream. The split jet near New Zealand possesses a large and very important component of the interannual variability in the South Pacific [e.g., Chen *et al.*, 1996; Kiladis and Mo, 1998; Frederiksen *et al.*, 1999]. The northern branch of the split jet has been shown to be influenced by tropical convection on intraseasonal time-scales [e.g., Hurrell and Vincent, 1991; Ko and Vincent, 1996].

[17] The strong pattern of interhemispheric correlation during August demonstrated with the NCEP/NCAR Reanalysis by Figures 1 and 2, however, does not appear to be present during other months. For the individual months June–September, Figure 3 shows the difference in average

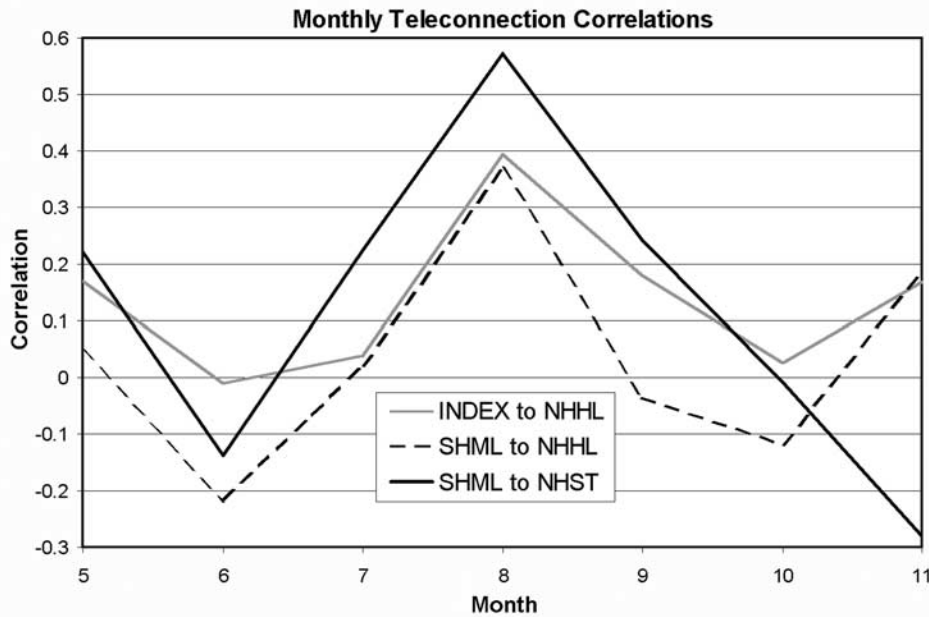


Figure 4. Correlations between monthly mean teleconnection anomalies and teleconnection index (see text for details) computed individually each month May–November.

surface pressure between averages of five separately selected years for each month June–September. The 5-year averages are taken for the highest pressure or the lowest pressure for the point at 40°S, 145°E. The selected years for July, as an example, are 1977, 1982, 1987, 1994, and 1997 with the highest surface pressure and 1978, 1981, 1990, 1995, and 1996 with the lowest surface pressure at the reference point in southeast Australia. The antiphase relationship of the middle latitudes near Australia to high southern latitudes is present for all 4 months from June to September. Station to station correlations (not shown) readily support the antiphase relationship. The SH pressure anomalies, however, are somewhat weaker in June and July than in August.

[18] The negative correlation of wintertime Australian pressure to that over the Southern Ocean to the south is consistent with the high latitude mode [Rogers and Van Loon, 1982]. More recently, Thompson and Wallace [2000] discuss the SH annular mode, which is to a rough approximation, zonally symmetric and displays opposite phases of anomalies on either side of 50–55°S. The alternating phase pattern in Figure 2, however, is localized, primarily confined between 110°E and 150°W in the SH.

[19] The NH component of the August pattern (Figure 3c), on the other hand, is not clearly present during June (Figure 3a) and July (Figure 3b). The September pattern (Figure 3d), however, does show some similarity in both hemispheres to the August pattern. The magnitudes of the September SH pressure anomalies near Australia and Antarctica are approximately equal to those of August, although the anomalies are shifted to the west during September. In the NH, there is also a slight enhancement by up to 2 hPa of the subtropical west Pacific pressure in Figure 3d. This feature, however, cannot be verified as statistically significant. The limited duration of the NH component indicates that the cross-hemisphere linkage is occurring on finer timescales than that of the more persistent ENSO.

3.2. Teleconnection Index

[20] An index is defined to measure the monthly intensity of the three main anomalies shown in Figures 1 and 2. It also allows us to define the positive and negative phases of the teleconnection. The index is calculated from a weighted sum of the observed sea level pressure at Dumont d’Urville (DUMONT) in Wilkes Land, Antarctica (66.67°S, 140.02°E), and reanalysis surface pressures averaged over 20–25°N and 125–140°E (NH subtropics (NHST)) and over 35–40°S and 135–150°E (SH middle latitude (SHML)),

$$INDEX = 0.495 \text{ NHST} + 0.275 \text{ SHML} - 0.171 \text{ DUMONT} - 599.07, \quad (1)$$

where the input is in hPa, and the value 599.07 is subtracted to bring the long term mean toward zero. The use of the monthly observations at Dumont d’Urville prevents the trends for high southern latitudes in the reanalysis from impacting the index. The intensity of a particular phase of the teleconnection is proportional to the magnitude of the index. The three weights are inversely proportional to the standard deviation of monthly surface pressure for August, so that the interannual variations at all three locations have an approximately equal effect on the teleconnection index. The average value of the five “positive Australia” Augusts for Figure 2 is 3.42, while that for the five “negative Australia” Augusts is –3.12.

[21] The linkage between the teleconnection and the extreme northern Pacific Ocean, suggested by Figure 2, can be examined by defining another anomaly, NH High Latitude (NHHL) for the region 160–170°W and 50–55°N near the Aleutian Islands. Figure 4 shows correlations during 1960–1999 computed individually for each month from May to November. For the Augusts during 1960–1999, the

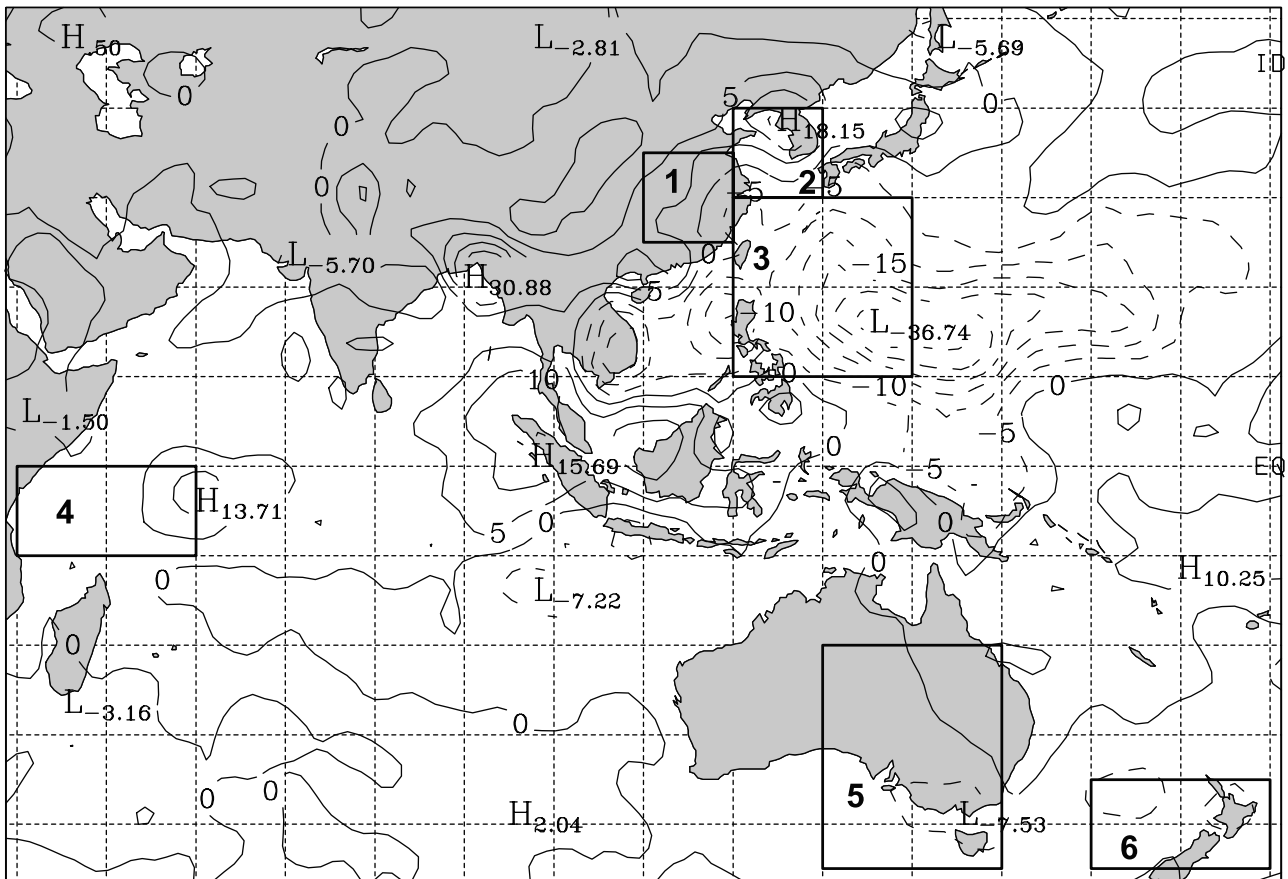


Figure 5. Map of difference in average Xie and Arkin precipitation (cm) during August between 5 years of above average surface pressure and 5 years of below average surface pressure at 40°S, 145°E. Contour interval is 2 cm. The boxes show precipitation regions 1–6 (see text for details).

correlation of NHHI to the teleconnection index and SHML are 0.40 and 0.37, respectively. Both of these correlations are significant at the 95% confidence level. The correlations are weaker and not statistically significant during other months, reflecting the limited duration of the teleconnection. Therefore, the August teleconnection extends from Antarctica on the southern edge to near the Arctic basin on the northern edge.

3.3. Precipitation

[22] The importance of the teleconnection to East Asian monsoon precipitation is revealed by Figure 5 which shows the difference in precipitation between Augusts of relatively high and low pressure over Australia. Gridded Xie and Arkin precipitation data are selected and averaged for two samples based upon the August surface pressure over southeastern Australia at the point 40°S, 145°E. We used the same five-August averages as in Figure 2. Figure 5 shows the difference in precipitation between the sample averages. Inland over China between about 30–35°N, precipitation is increased by as much as 12.6 cm during positive phase Augusts compared to negative phase Augusts. Precipitation is likewise increased over Korea with a maximum of almost 20 cm. To the south, precipitation is decreased over the northern Philippines.

[23] Due to the large interannual variability in precipitation, the statistical significance of the Figure 5 pattern is

difficult to show on a point-by-point basis. We choose the following method to demonstrate that the teleconnection is linked to significant changes in precipitation for the East Asian monsoon and elsewhere. The teleconnection index for each month July, August, and September during 1979–1999 is correlated to the area-averaged precipitation during the same month for six regions: (1) near China for 110–120°E, 25–35°N, (2) near Korea for 120–130°E, 30–40°N, (3) near the Philippines for 120–140°E, 10–30°N, (4) over the western tropical Indian Ocean for 40–60°E, 0–10°S, (5) near eastern Australia for 130–150°E, 20–45°S, and (6) near New Zealand for 160–180°E, 35–45°S. The regions are shown by the heavy shaded areas in Figure 1 and the boxes in Figure 5. Results of the correlation are displayed in Table 1 for each of the months July, August, and September. Only results significant at the 90% confidence level or better are shown. No significant correlations are found to the teleconnection index or NHST during July. Consequently, these values are not included in Table 1. Significant correlations are much more easily found during August than during July or September. This time variation is consistent with intraseasonal timescales. The time duration is not surprising given that the summertime North Pacific Subtropical High near NHST has a strong intraseasonal modulation [e.g., Wang and Xu, 1997]. The correlation between SHML and the precipitation in region 3 near the Philippines changes sign between July and August, indicative of the

Table 1. Correlation of Area-Averaged Xie and Arkin Merged Precipitation to Teleconnection Anomalies

Region	Description	Location	Teleconnection index		NHST		SHML	
			August	September	August	September	July	August
1	China	110–120°E 25–35°N	0.51		0.68	0.46		0.44
2	Korea	120–130°E 30–40°N	0.57		0.59	0.52		0.59
3	Philippines	120–140°E 10–30°N	–0.57	–0.50	–0.42	–0.48	0.53	–0.53
4	Western tropical Indian Ocean	40–60°E 0–10°S	0.47					0.52
5	Eastern Australia	130–150°E 20–45°S	–0.66				–0.55	–0.80
6	New Zealand	160–180°E 35–45°S	–0.68					–0.73

All correlations shown are statistically significant at 90% confidence or better. No significant correlations between the precipitation regions and the teleconnection index are found for July.

different behavior between months. The August precipitation in all six regions is correlated to the teleconnection index as well as the teleconnection anomaly in the mid-latitudes of the SH. The positive correlations, 0.51 and 0.57, during August between the teleconnection index and precipitation zones, 1 and 2, respectively near China and Korea support the positive contours seen in these regions for Figure 5. Within these zones, precipitation during extreme negative phases of the teleconnection averages about 75–80% of that during positive extremes. The negative correlation, –0.57, to region 3 during August also supports the negative difference for that region in Figure 5. The positive correlation between precipitation in regions 1 and 2 to the NHST anomaly is physically realistic as an increased subtropical high over the western Pacific can increase the southerly flow of moist area over East Asia. Furthermore, the August precipitation over eastern Australia and New Zealand is highly correlated to SHML, as precipitation there is reduced when the local pressure is relatively high. Thus the teleconnection links variations in August precipitation over the West Pacific sector.

3.4. Tropical Circulation

[24] A connection between the West Pacific pattern and the tropical circulation is suggested by correlation of the teleconnection index to tropical precipitation. Table 1 shows that the August correlation is positive for region 4 over the western tropical Indian Ocean and negative for region 3 over the western Pacific Ocean near the Philippines. The tropical east–west vertical circulation associated with the teleconnection is displayed in Figure 6 which shows the horizontal velocity and the difference in both horizontal velocity and velocity potential at the 850 hPa and 200 hPa levels. The 5-year averages are the same as for Figure 2. The observed teleconnection appears to be the result of tropical convection on intraseasonal timescales [Kiladis and Mo, 1998]. Not only is the time duration of the teleconnection consistent with intraseasonal timescales, the tropical pattern in Figure 6 also appears similar to phases of the MJO shown by Hendon and Salby [1994] and Maloney and Hartmann [1998]. When the surface pressure is above normal over Australia, the lower-tropospheric winds at 850 hPa have an increased easterly component extending from the maritime continent to eastern equatorial Africa

(Figure 6d), while the difference winds in the upper troposphere at 200 hPa are westerly near the Equator from about 80°E to 160°E (Figure 6c). Furthermore, the difference winds at 850 hPa show anticyclones in the subtropical western Pacific in the NH and near southeastern Australia in the SH (Figure 6d). These anticyclones can be linked with the tropical ISO [e.g., Kiladis and Weickmann, 1992; Hendon and Salby, 1994].

[25] Kiladis and Mo [1998] display a teleconnection with a wind pattern strikingly similar to that in Figures 6c and 6d. They use the NCEP/NCAR Reanalysis fields for May–September filtered to motions on timescales of 30–70 days. Velocity and outgoing longwave radiation (OLR) anomalies are associated with the phase of the tropical ISO and with enhanced convection in the western tropical Pacific sector. In their Figures 8.12b and 8.12c, they show 200 hPa and 850 hPa velocity patterns, respectively that resemble those from the phase of the August teleconnection that corresponds to below average pressure for Australia. The anomalies of Kiladis and Mo [1998] have a baroclinic structure at low latitudes and an equivalent barotropic structure in the extratropics, consistent with the findings of the current study. Furthermore, the 500 hPa geopotential height anomalies displayed in their Figure 8.13 are analogous to the surface pressure anomalies in the middle and high latitudes of the SH shown in Figure 2 of the current study. Thus, the three primary anomalies (high-latitude SH, midlatitude SH, and subtropical NH) seen in Figure 2 are similar to patterns shown by Kiladis and Mo [1998]. They indicate that their pattern results from outflow from the tropical convection enhanced by the ISO. The ability of divergent advection from tropical convective anomalies to generate circulation anomalies in the subtropics is explained by Tyrrell *et al.* [1996] with vorticity budget calculations. Similarly, Sardeshmukh and Hoskins [1988] emphasize the importance of divergent outflow from tropical convection in generating nonlocal responses.

[26] The similarity of the August teleconnection displayed in Figures 1, 2, and 6 to ISO phenomena is consistent with the findings of Wang and Xu [1997]. They find a northwestward or westward propagating convective anomaly that displays phase-locking to subseasonal variations in the East Asian summer monsoon. The oscillation, which they refer to as the climatological intraseasonal oscillation (CISO), is linked with OLR extrema over the

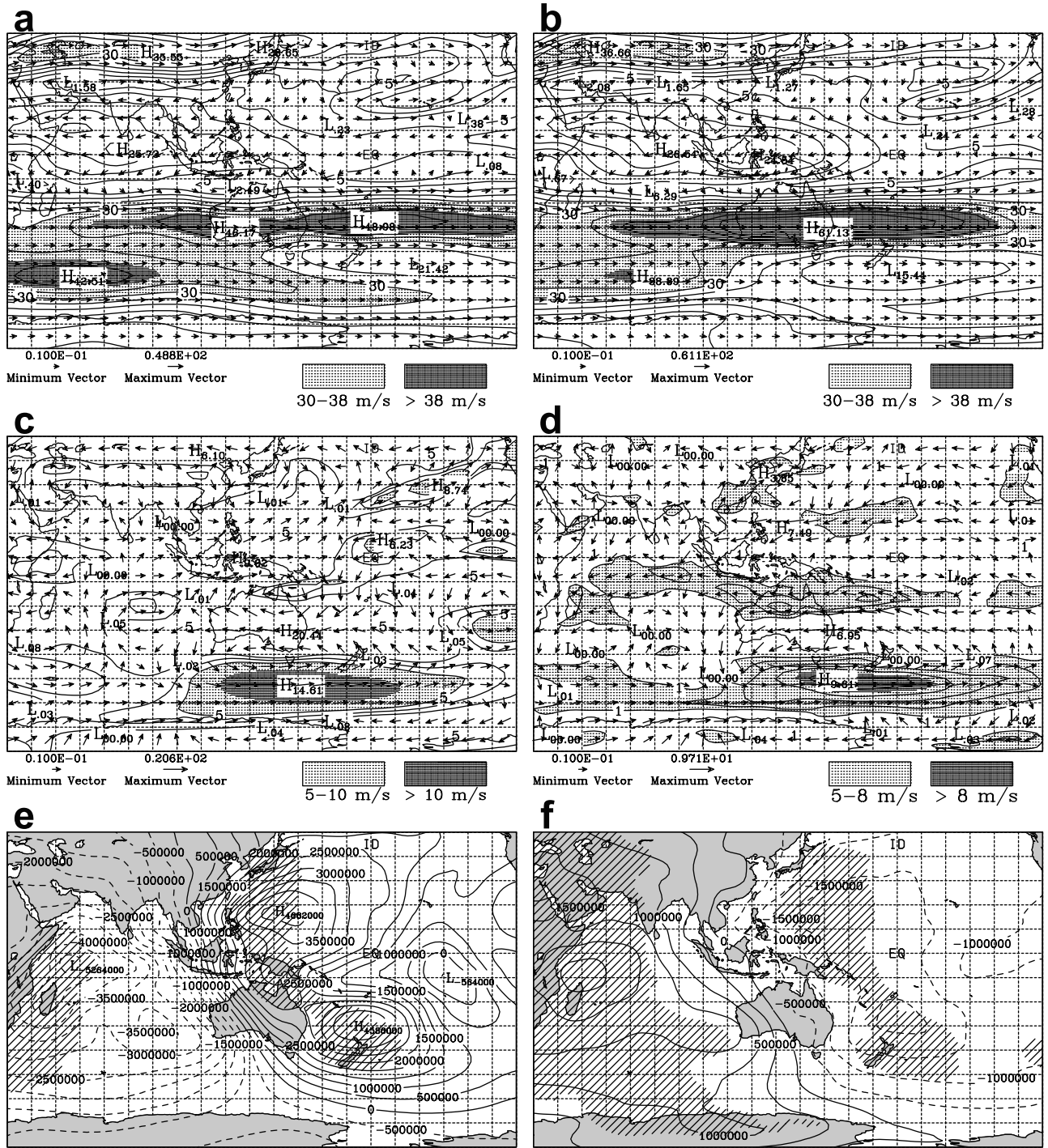


Figure 6. Maps of August horizontal velocity (m s^{-1} , arrows) and wind speed (contours, m s^{-1} at (a) 200 hPa for five Augusts of highest pressure at 40°S, 145°E and (b) 200 hPa for five Augusts of lowest pressure at 40°S, 145°E; difference in horizontal velocity and wind speed at (c) 200 hPa and (d) 850 hPa; and difference in velocity potential (contours, $\text{m}^2 \text{s}^{-1}$) at (e) 200 hPa and (f) 850 hPa. Contour intervals are 5 m s^{-1} for (a) and (b), 2 m s^{-1} in (c) and (d), and $5 \times 10^5 \text{ m}^2 \text{s}^{-1}$ in (e) and (f). Wind speed between 30 and 38 m s^{-1} is light shaded and greater than 38 m s^{-1} is heavy shaded in (a) and (b). Wind speed between 5 and 10 m s^{-1} in (c) and (d) light shaded and greater than 10 m s^{-1} in (c) and 8 m s^{-1} in (d) is heavy shaded.

western Pacific near 15°N, 140°E. Wang and Xu [1997] also show that the amplitude of CISO peaks during August and September, the same time of year when the teleconnection can be seen in Figure 3.

[27] A dipole or seesaw in vertical circulation with alternating centers of rising and sinking motion between the Indian Ocean and the western tropical Pacific is commonly seen with the tropical ISO [e.g., Lau and Chan,

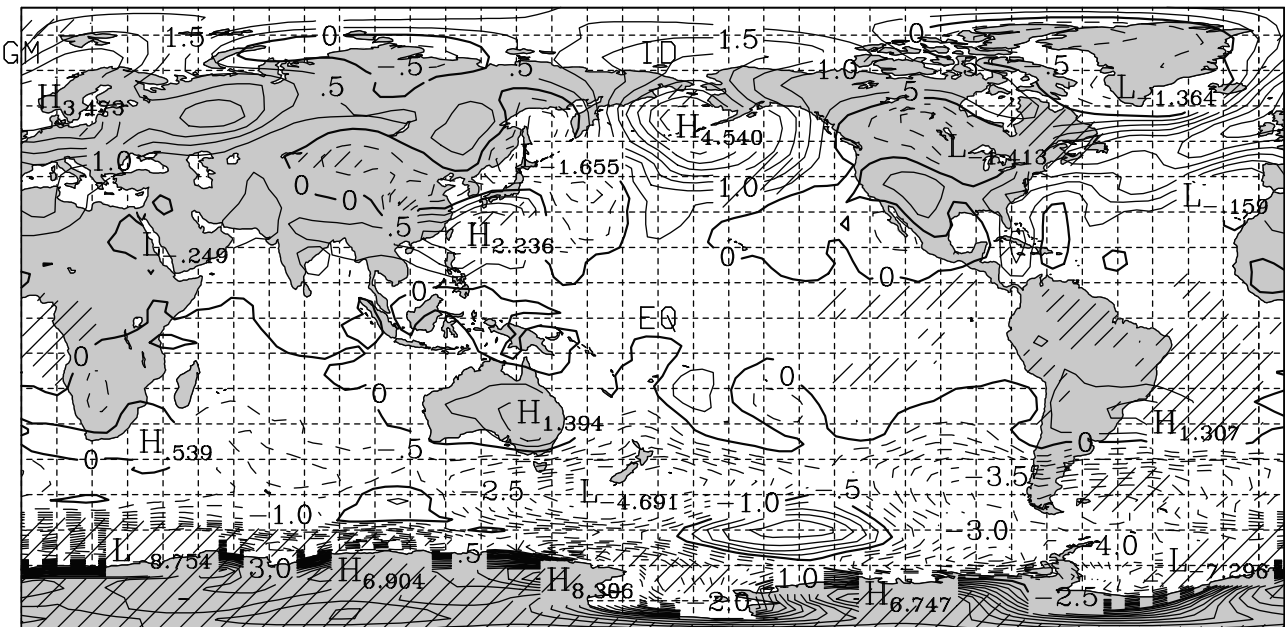


Figure 7. Surface pressure difference (hPa) between the CCM2 simulation without Antarctic sea ice (NSIS) and the control (CNT). Contour interval is 0.5 hPa. Negative contours are dashed. Thick contour is 0. Hatched areas are statistically significant at 95% according to the Student's t-test. Latitude and longitude dashed lines are spaced every 10°.

1986; Zhu and Wang, 1993]. A similar dipole is seen in the velocity potential field displayed in Figures 6e and 6f for 200 hPa and 850 hPa, respectively. As the divergent component of the horizontal wind flows from low to high values of the velocity potential, lower-tropospheric convergence, upper-tropospheric divergence and middle-tropospheric ascent can be inferred over the western Indian Ocean. This is consistent with increased precipitation in region 4 for the positive phase of the teleconnection. The descending branch of the circulation is over the western Pacific Ocean, consistent with the negative correlation of the teleconnection index to precipitation in regions 3, 5, and 6.

[28] Over the midlatitude Indian and South Pacific Oceans, Figure 6a shows that the westerly polar front jet is greatly enhanced between 45°S and 65°S during years with increased pressure over southeastern Australia as compared to Figure 6b. The velocity differences in the upper troposphere (Figure 6c) and lower troposphere (Figure 6d) show an equivalent barotropic structure with the vectors in a westerly direction and having a maximum magnitude of 9.6 m s^{-1} at 850 hPa and 14.6 m s^{-1} at 200 hPa. In contrast, the westerly subtropical jet is significantly weakened near Australia when the pressure is high over southeastern Australia. Thus, Figure 6 demonstrates the linked behavior between the tropics and SH middle latitudes.

4. NCAR CCM2 Results

4.1. West Pacific Interhemispheric Teleconnections

[29] Numerical simulations with the NCAR CCM2 produce a late boreal summer/austral winter teleconnection that is strikingly similar to the observed phenomenon described

in section 3. Whereas the observed teleconnection is associated with tropical convection, the modeling results originate from forcing near Antarctica. The CCM2 is described in detail by Hack *et al.* [1993], while Antarctic sensitivity simulations are discussed by Bromwich *et al.* [1998a, 1998b] and Lubin *et al.* [1998]. The simulations are performed with version 2.1 of CCM2, which has a standard horizontal resolution of T42 ($2.8^\circ \text{ latitude} \times 2.8^\circ \text{ longitude}$) and 18 levels in the vertical. The model reasonably captures most climatic features in southern high latitudes, even though it has a simplistic treatment of sea ice [e.g., Tzeng *et al.*, 1994; Hack *et al.*, 1994]. The 15-year seasonal cycle simulation that Bromwich *et al.* [1998a] called NSIS has monthly Antarctic sea ice replaced throughout the year by open water at -1.9°C . Otherwise, sea surface temperature is climatological. Permanent Antarctic ice shelves are retained in NSIS. The results of this sensitivity experiment are compared to a control run (CNT) conducted with the monthly climatological parameter settings. The simulation CNT includes seasonal variation of specified sea ice and sea surface temperature without any interannual variations in the boundary conditions. Each simulation generates 15 years of monthly average fields.

[30] Figure 7 shows the surface pressure difference between NSIS and CNT averaged over all Septembers of the 15-year runs. September is the month of maximum SH sea ice in CNT. Hatching shows statistically significant differences at the 95% confidence level according to the Student's t-test. Similar to the modeling results of Simmonds and Budd [1991], the surface pressure is reduced in NSIS over most of the Southern Ocean near Antarctica in response to the sea ice removal. Figure 7 shows pressure anomalies of opposite sign between Australia and the latitudes to the south, similar to Figure 3.

[31] The September pattern in Figure 7 contains three anomalies over Australia and the western Pacific that appear similar to August fields displayed in Figures 1 and 2. In the NH there are statistically significant anomalies over the subtropical western Pacific near 25°N, 130°E, where the pressure is increased by up to 2.2 hPa, and inland over northern China and near Mongolia, where the pressure is decreased by 1–3 hPa. The location of the anomalies and the ratio of their magnitudes do show differences between Figures 2 and 7. Some of the difference in anomaly magnitudes between Figures 2 and 7 result because Figure 2 is the difference between extremes, while Figure 7 is the difference between an extreme sea ice simulation and a control based on climatology. The magnitude of the high anomaly near Australia in Figure 7 is much weaker relative to the negative anomaly to the south compared to those of Figure 2. Another difference between Figures 2 and 7 is the large contribution to zonal wave number 1 to the positive anomaly near Australia in Figure 2 while the analogous anomaly in Figure 7 is associated primarily with wave number 2.

[32] The pressure differences near Asia in Figure 7 impact the East Asian monsoon. The close relationship of the southwest Pacific subtropical high and patterns of precipitation over China is discussed by many researchers [e.g., *Lau et al.*, 1988; *Wang and Li*, 1990; *Samel et al.*, 1999]. *Bromwich et al.* [1998a] find that the pressure difference in Figure 7 is linked with a northward shift of the September large-scale precipitation over China. They show that some of the affected grid points have statistically significant increases or decreases in large-scale precipitation by as much as 6 cm. The year-to-year change in monsoon precipitation is a critical feature of the climate variability for China [e.g., *Lau and Li*, 1984; *Fan and Oglesby*, 1996; *Park and Schubert*, 1997]. The very large change in simulated monsoon precipitation over China, however, is probably exaggerated by the excessive convective precipitation produced by CCM2 [*Hack et al.*, 1994; *Kiehl*, 1994]. Another consequence of excess CCM2 precipitation may include the simulated rainy season lasting later into the seasonal cycle. September is normally very late in the cycle of the observed summer monsoon [*Domrös and Peng*, 1988]. Considering the large amount of precipitation simulated by CCM2, the September results in Figure 7 may represent an example of a late summer monsoon case that best matches the observed case slightly earlier in the seasonal cycle. Thus, despite apparently different forcings, the CCM2 teleconnection patterns within the pressure difference fields over the western Pacific during a late austral winter month show a large similarity with the observed teleconnection fields at about the same time of year.

4.2. Tropical Component

[33] Similarities between the modeled phenomenon and that observed are also seen in the tropical fields. Figure 8 shows the NSIS–CNT difference horizontal winds and velocity potential on CCM2 sigma surfaces in the upper troposphere (sigma = 0.1892) and the lower troposphere (sigma = 0.8664). These sigma levels are usually close to 200 hPa and 850 hPa, respectively. Figure 8 displays some noise in the NSIS–CNT difference wind field within the tropics. Nevertheless, westerlies over the Indian Ocean and

easterlies along 140–170°E over the Pacific Ocean are evident between 5 and 15°N in the upper troposphere. This wind pattern resembles stages of the life cycle of intra-seasonal tropical circulations shown by *Hendon and Salby* [1994] and *Maloney and Hartmann* [1998]. Consistent with the baroclinic structure of many tropical circulations, the lower tropospheric winds along the Equator in Figure 8b display a tendency to be in the opposite direction to those in the upper troposphere, as there are easterlies between 0 and 25°N over India and the Indian Ocean. Near the Philippines, the winds are northeasterly in the lower troposphere and southwesterly in the upper troposphere. Moreover, to the northeast of the easterlies at sigma = 0.8664 across southern Asia, there is anticyclone centered near 25°N, 120°E. There is also an anticyclone centered over southeast Australia.

[34] The differences between the NSIS and CNT simulations in the tropics resemble the observed differences between the phases of the teleconnection. Furthermore, the length of persistence of the NH anomalies shown in Figure 7 suggests that the cross-hemisphere teleconnection is occurring on intraseasonal timescales. *Slingo et al.* [1996] noted that while all global climate models have difficulty accurately simulating the tropical ISO, CCM2 is one of only 3 out of 15 GCMs tested to capture the amplitude of the ISO. *Wang and Schlesinger* [1999] attribute the success of CCM2 in simulating the ISO amplitude to its nonpenetrating convection parameterization. *Maloney and Hartmann* [2001] show that CCM2's convection parameterization is superior to that of the more recent CCM3 for simulations of the MJO.

[35] The velocity potential fields in Figures 8c and 8d show a similar dipole in the vertical circulation to observed field in Figure 6, as there is lower-tropospheric convergence and upper-tropospheric divergence over Africa and the western Indian Ocean and vice versa over the western tropical Pacific. Thus the NSIS–CNT difference velocity field includes rising (sinking) over the western Indian Ocean and Africa (western Pacific). There is an additional center of upper-tropospheric convergence and lower-tropospheric divergence near the surface pressure maximum over Australia. The modeled pattern of the tropical vertical circulation is, in general, physically consistent with the influence of the tropical ISO on precipitation, divergence and humidity shown by *Hendon and Salby* [1994] and *Maloney and Hartmann* [1998]. Moreover, the tropical and NH subtropical difference circulation in Figure 8 is highly consistent with the alternating phases of the CISO shown by *Wang and Xu* [1997]. Although the CCM2 modeling results and the observed teleconnection have different forcings, the similarity in results does suggest that both reflect a similar favored response pattern in the western Pacific region on intraseasonal timescales.

4.3. Antarctic Cloud Simulations

[36] A somewhat different set of CCM2 simulations provides another example of Antarctic forcing that results in a pattern appearing similar to the observed teleconnection. Previously, *Lubin et al.* [1998] used CCM2 to demonstrate that significant remote impacts result from improvements to the radiative properties of Antarctic clouds. Their simulations did not have the annual cycle. Instead, perpetual January (austral summer) boundary con-

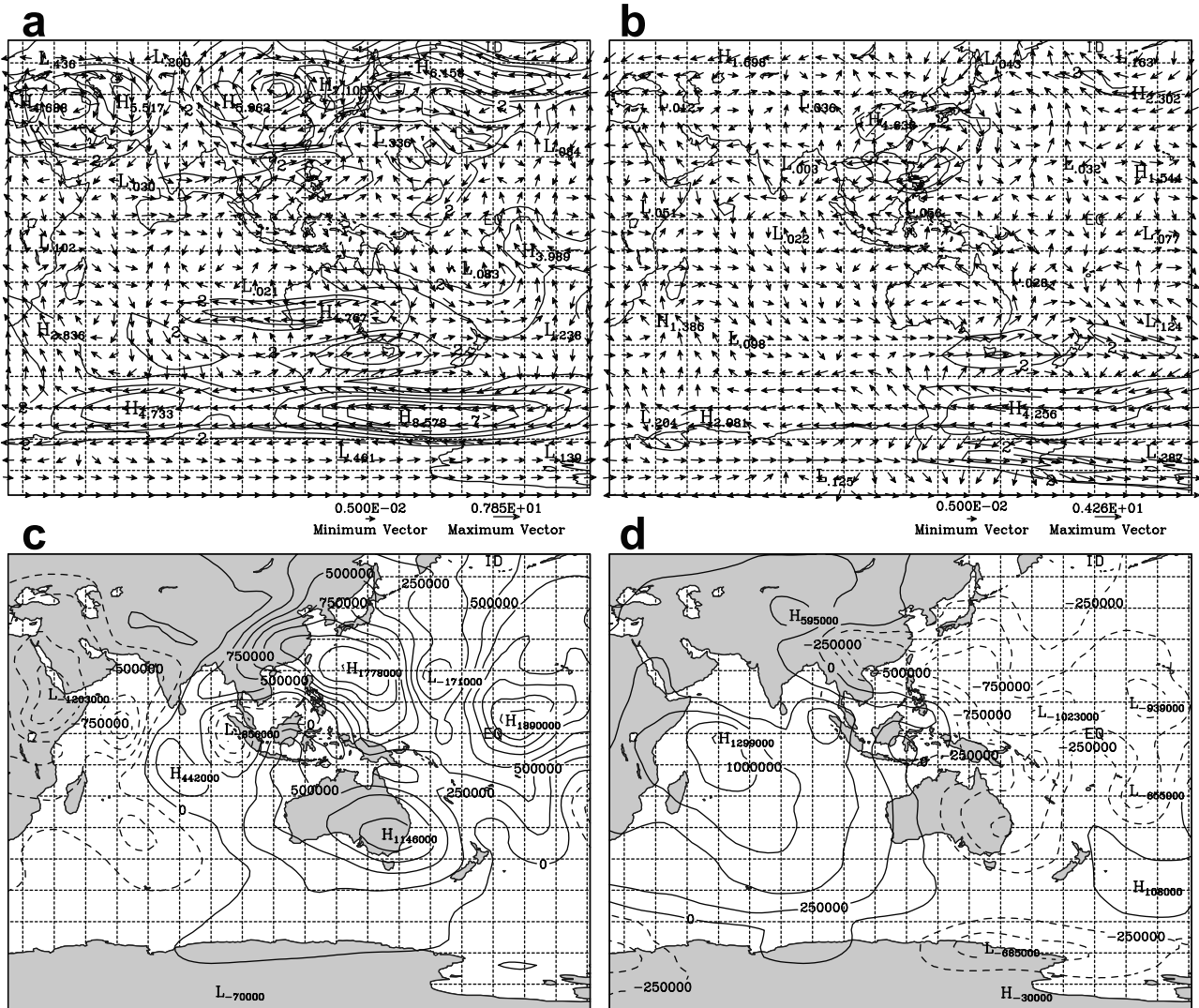


Figure 8. The difference NSIS–CNT in horizontal velocity (vectors, m s^{-1}) and velocity potential (contours, $\text{m}^2 \text{s}^{-1}$) on CCM2 sigma levels for September: (a) horizontal velocity at sigma = 0.1892, (b) horizontal velocity at sigma = 0.8664, (c) velocity potential at sigma = 0.1892, and (d) velocity potential at sigma = 0.8664. Contours are wind speed (m s^{-1}) in (a) and (b) every 1 m s^{-1} . Contour interval is $2.5 \times 10^5 \text{ m}^2 \text{s}^{-1}$ in (c) and (d).

ditions are employed. Consequently, both longwave and shortwave radiative characteristics of Antarctic clouds were important. For the current study, two CCM2 simulations are performed with perpetual August (austral winter) boundary conditions including climatological sea ice and sea surface temperature for August. While August is one of the most climatologically stable months, the simulations are, nevertheless, impacted by the lack of forcing with the seasonal cycle. The first simulation is a 12-month control simulation with only standard CCM2 water clouds [Hack *et al.*, 1993]. The second simulation is a 12-month sensitivity experiment in which the radiative properties of water clouds over continental Antarctica are replaced by Ebert and Curry's [1992] parameterization for ice clouds. Observations indicate that the sensitivity simulation is more realistic as Antarctic clouds consist primarily of ice particles. Lubin *et al.* [1998] explain in detail the reasoning for the change in radiative properties. In the sensitivity experiment, the stand-

ard CCM2 parameterization for water clouds is applied north of continental Antarctica. Boundary conditions are identical for both runs. Therefore, the difference between the simulations originates from Antarctic clouds and is dominated by longwave radiative effects during the Polar Night. The first 2 months of the perpetual August simulations are taken as an adjustment period. Only the last 10 months are analyzed here. In both the August case presented here and the January case discussed by Lubin *et al.* [1998], the change in radiative properties increases the surface temperature (not shown) by a few degrees over Antarctica.

[37] Figure 9 shows the average difference in surface pressure between the Antarctic ice cloud simulation and the control for August. In high southern latitudes, the difference in surface pressure induced by the cloud radiative changes is about one-third the magnitude of the large positive anomalies simulated by Lubin *et al.* [1998] during January. Pressure reductions in the ice cloud simulation are about

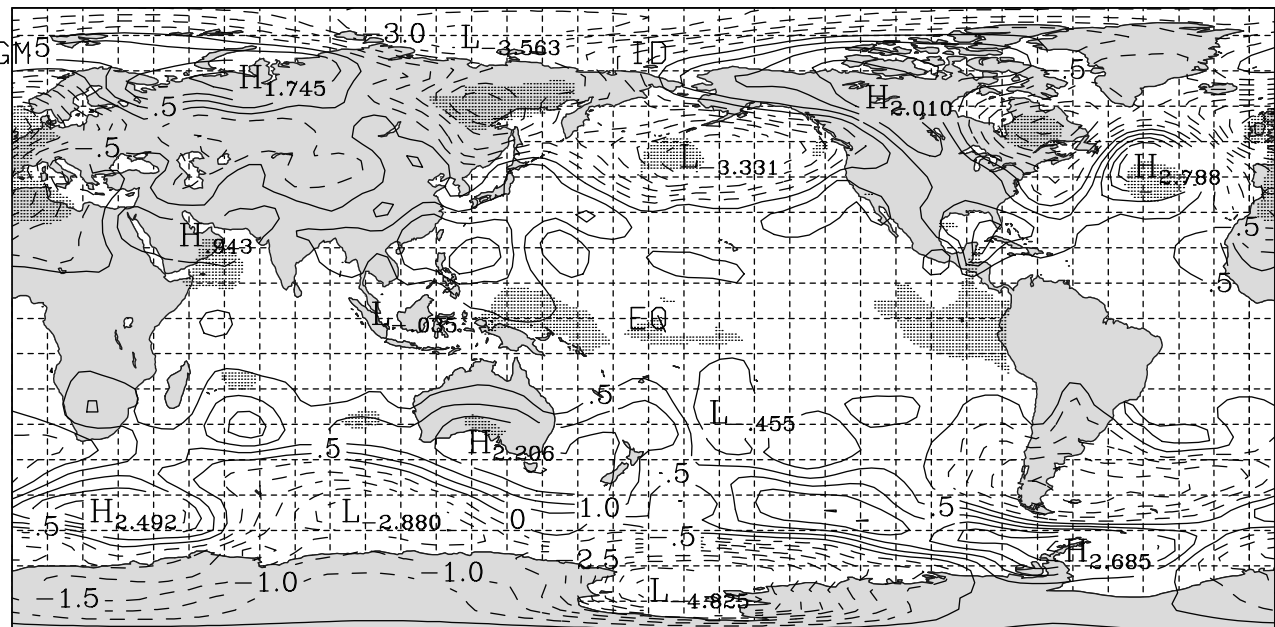


Figure 9. The average difference in surface pressure (hPa) between the Antarctic ice cloud and the water cloud simulations for August. Contour interval is 0.5 hPa. Shaded areas are statistically significant at 95%.

1–2 hPa over the Antarctic coast, up to 4.8 hPa over the Ross Sea near 75°S, 180° and by about 2.9 hPa at 55°S, 95°E in the Indian Ocean. On the other hand, pressure increases by about 2.5 hPa over the northern Antarctic Peninsula. The general pressure decrease south of 60°S is not large enough to be verified as a statistically significant response to the changes in cloud radiative properties. Nevertheless, Figure 9 does show the tendency for a three anomaly pattern in the western Pacific sector extending northward from the Ross Sea area to the NHST. The pressure falls near Antarctica are compensated by a general pressure increase in SH midlatitudes, although the pressure does decrease over southern South America and the Atlantic Ocean near 45°S. Over southern Australia, there is a statistically significant pressure increase by 1–2 hPa. Both Figures 7 and 9 show a localized similarity to the high latitude mode with a positive anomaly near Australia and a negative anomaly near Antarctica. This SH pattern is shifted about 10° to the north in Figure 7, perhaps because the differential forcing is over the Southern Ocean in the sea ice experiment and over continental Antarctica in the cloud experiment. Both the difference patterns in Figures 7 and 9 also show increases in surface pressure over the subtropical western Pacific Ocean in the NH.

[38] Thus, Figure 7 for September in the annual cycle simulation and Figure 9 for the perpetual August simulation have approximately similar three-anomaly patterns in the western Pacific sector, even though the Antarctic forcing and local responses are not identical. The horizontal and vertical components of the tropical circulation for the perpetual August experiment (not shown) also resemble the corresponding fields for the sea ice experiment in Figure 8. Two different cases, the sea ice removal simulations and the Antarctic cloud simulations, show a very similar link between Antarctic forcing and simulated pressure variations

in the NHST. Furthermore, analogous to the September results of the sea ice removal experiment found by Bromwich *et al.* [1998a], large-scale precipitation is increased in northern China (not shown) in the Antarctic ice cloud simulation for August. The anomalous tropical vertical and horizontal circulations (not shown) induced by the change from water to ice clouds are also similar to those shown in Figure 8 for the sea ice removal experiment. Thus, with two different CCM2 scenarios, monthly average fields for late boreal summer show that simulated teleconnections originates from high southern latitude forcing and suggest a link to the tropical ISO. Therefore, it appears that modeling studies capture similar phenomena to that observed and can be used to study the teleconnection. The preference for the modeled teleconnection to appear 1 month later (September) in the CCM2 sea ice experiment could be related to the excessive strength of the simulated monsoon precipitation for East Asia during late summer when the observed monsoon circulation is beginning to change toward the winter phase of dry northerly winds [Domrös and Peng, 1988].

5. Development of the Teleconnection on Intraseasonal Timescales

[39] The development of the observed teleconnection needs to be examined on finer timescales than those resolvable with the monthly mean fields previously shown. The monthly means suggest that the teleconnection persists about 1 month, consistent with an intraseasonal duration. Furthermore, the teleconnection shows resemblance to known MJO response patterns. In place of the monthly observations from Dumont d'Urville and monthly values of NHST and SHML from the NCEP/NCAR Reanalysis in (1), daily fields from the NCEP/NCAR Reanalysis are used to detail the development of the teleconnection over the intra-

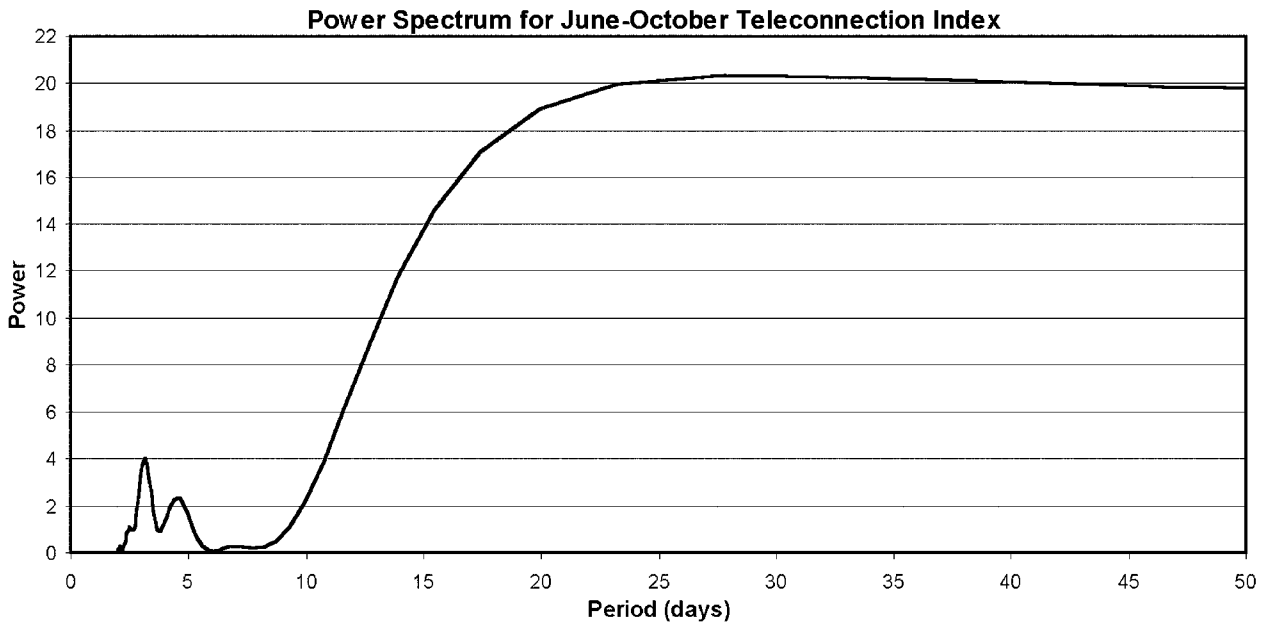


Figure 10. Power spectral density of the adjusted teleconnection index values during June–October for 1979–1999.

seasonal timescale. The daily fields show linkage between OLR and the three main teleconnection anomalies on the intraseasonal timescale. Tropical convection associated with OLR anomalies can provide the forcing to generate the observed teleconnection. The analysis presented here will also help us understand the preference for the teleconnection to appear in monthly mean fields for August.

[40] Daily values of mean sea level pressure are taken from NCEP/NCAR Reanalysis for the months June–October during 1977–1999. With the sea level pressure, we can approximate the teleconnection index on a daily basis. An adjusted teleconnection index is calculated with a weighted sum of daily sea level pressures. A contribution from Southern Ocean grid point (SH high latitude (SHHL*)) at 140°E, 65°S located slightly north of Dumont d’Urville replaces observations of the monthly pressure from that Antarctic station. The adjusted teleconnection index also incorporates the average pressures for an area in the Australia–New Zealand sector of the SH midlatitudes (SHML*) for 35–40°S, 135–150°E, and an area offshore of Asia over 20–25°N, 125–140°E in the Northern Hemisphere subtropics (NHST*),

$$INDEX^* = 0.495 NHST^* + 0.275 SHML^* - 0.171 SHHL^* - 610, \quad (2)$$

where the input is in hPa, and 610 hPa are subtracted to bring the mean toward zero.

[41] Figure 10 shows the power spectrum for the adjusted teleconnection index during June–October of 1977–1999. There is a peak in the spectrum for frequencies near a 30-day period. Large contributions to the variance are also present for periods longer than 30 days, so it is entirely possible for one phase of the teleconnection to dominate a monthly mean. Consistent with its similarity to known MJO meteorological

fields, the teleconnection is very active on intraseasonal timescales. Figure 10 demonstrates that an intraseasonal examination of the teleconnection is appropriate.

[42] To help explain the preference for the teleconnection in August fields, we evaluated the autocorrelation of the daily adjusted teleconnection index for each of the months June, July, August, September, and October. Figure 11 shows the autocorrelation for lags of up to 20 days. The autocorrelation for the month of August is clearly larger over a broad range of lags than for the other months. The least autocorrelation is typically occurs during October. The relatively large persistence of the teleconnection index during August helps explain why the teleconnection is clearly seen for this month in Figure 3c and not clearly seen for other months.

[43] Daily values of geopotential height and horizontal velocity on isobaric surfaces were also obtained from the NCEP/NCAR Reanalysis during 1977–1999 including 10 years with Augusts of extreme value (magnitude greater than 2 hPa) for the teleconnection index. The divergent component was obtained from the velocities. The analysis concentrated on velocities at 850 hPa and 300 hPa, and geopotential heights at 850 hPa. Additionally, interpolated daily outgoing longwave radiation (OLR) data from the National Oceanic and Atmospheric Administration (NOAA)-CIRES for 1974–2001 was obtained on a 2.5° longitude by 2.5° latitude grid from their web site at <http://www.cdc.noaa.gov/>. The OLR data are a good measure of tropical convection to which they are negatively correlated.

[44] Time filtering has been performed on the data to extract the intraseasonal component. The data cover the 151 days starting on 2 June and ending on 30 October. The mean and the linear trend are separated from the data, and the remainder can be filtered for variations on the intraseasonal timescale (roughly 2 weeks to 3 months). The

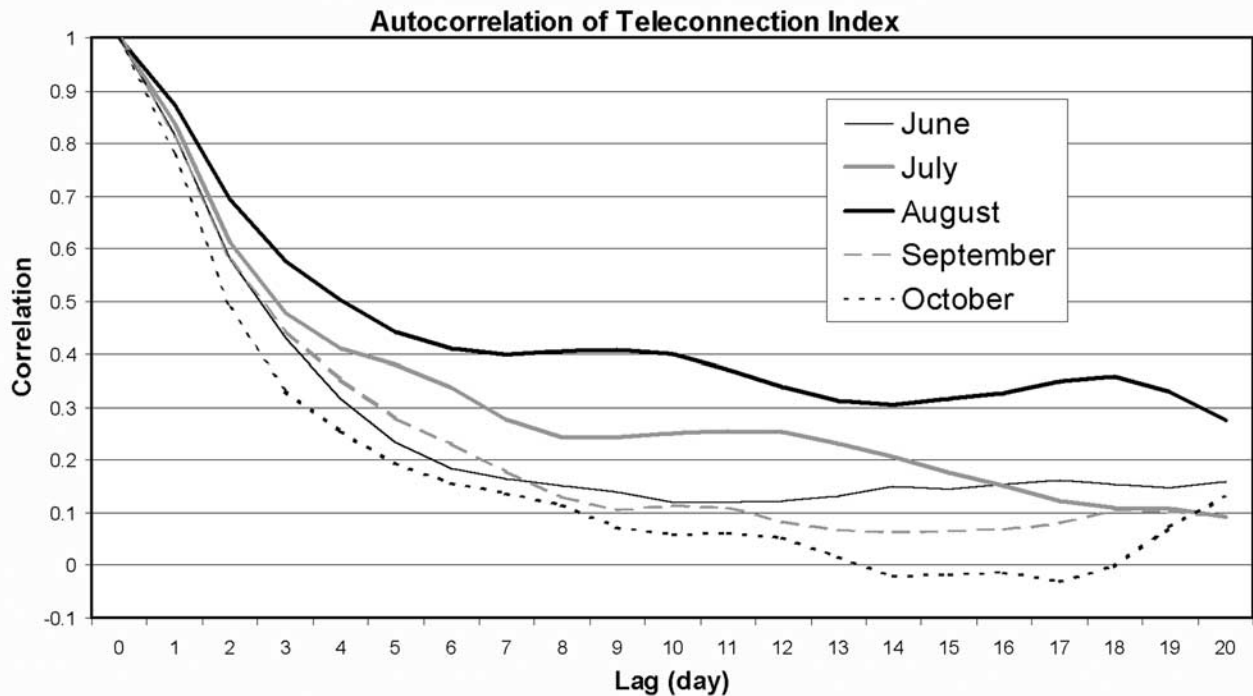


Figure 11. Autocorrelation of adjusted teleconnection index for each month June–October over lags 0–20 days.

longest unfiltered periodicity is 150 days. Time series (not shown) of the adjusted teleconnection index, OLR and the teleconnection sea level pressure anomalies filtered to variations with a period of 25–75 days suggest coordination between the individual teleconnection anomalies, and between the anomalies and OLR. The time series also suggest recurring seasonal development patterns for each of the positive and negative phases of the teleconnection. Therefore, we can study the development of the teleconnection by averaging similar events.

[45] To verify the link between tropical convection and the pressure anomalies of the teleconnection index, we correlated the OLR in the NH tropical sector 5–20°N, 100–115°E to the individual teleconnection pressure anomalies and to the adjusted teleconnection index. This sector, near Thailand, Malaysia, and Indonesia, is shown by the dashed box in Figure 14, presented later. A preliminary analysis suggested that correlations to OLR were particularly high for this NH tropical sector. The June–October fields were filtered to oscillations with periods of 25–75 days. Kiladis and Weickmann [1992] and Kiladis and Mo [1998] note that similar filtering is a reasonable way of isolating MJO effects. After the filtering, the August values from 1979–1997 are used to compute correlations with lags from –20 to 20 days. When the filtered OLR anomalies lead (follow) the filtered pressure anomalies, the lag is referred to as positive (negative). Only correlations significant at 95% confidence are displayed in Figure 12. The filtered correlations reflect the variations on intraseasonal timescales. The largest correlation magnitudes are found when the sector OLR leads the teleconnection pressure anomalies, thus the lag is positive. This indicates the teleconnection anomalies represent a extratropical response to

the tropical convection. Extreme values of the correlation coefficient between the adjusted teleconnection index and sector OLR are 0.58 for a lag of 10 days and –0.36 for a lag of –13 days. Thus the maximum positive phase of the teleconnection, characterized by positive pressure anomalies for NHST* and SHML* and a negative pressure anomaly for SHHL*, is frequently preceded by a positive OLR anomaly (reduced convection) for the tropical sector. The OLR near Indonesia may have an intermediate-scale predictive value for both the NH and SH. There is also a tendency for a positive anomaly of the teleconnection index to be followed by a negative anomaly of OLR, though the correlation is weaker for negative lags. Furthermore, there are significant correlations of August OLR to August values of all three teleconnection pressure anomalies in Figure 12. Correlations between the pressure anomalies indicate that the SHHL* anomaly slightly leads the SHML* anomaly. Both the SH anomalies lead the NHST* anomaly.

[46] Compositing of similar phases of the teleconnection is now performed to help understand the temporal development of the phases. From the teleconnection index as defined in section 3.2, we identify individual Augusts of extreme positive and negative phase. The extreme years are taken as years when the magnitude of the index exceeds 2 hPa. We select the 5 positive extreme years: 1982, 1987, 1993, 1994, and 1995, and 5 negative extreme years: 1981, 1984, 1990, 1991, and 1992. Some of the positive years are associated with El Niño warm events in the Pacific Ocean. Figure 13 shows the composite development of the 850 hPa geopotential height field for the 5 positive index years. The climatology for each day during 1977–1999 has been subtracted from the height fields which are then filtered to include variations with periods of 15 days or longer. Both

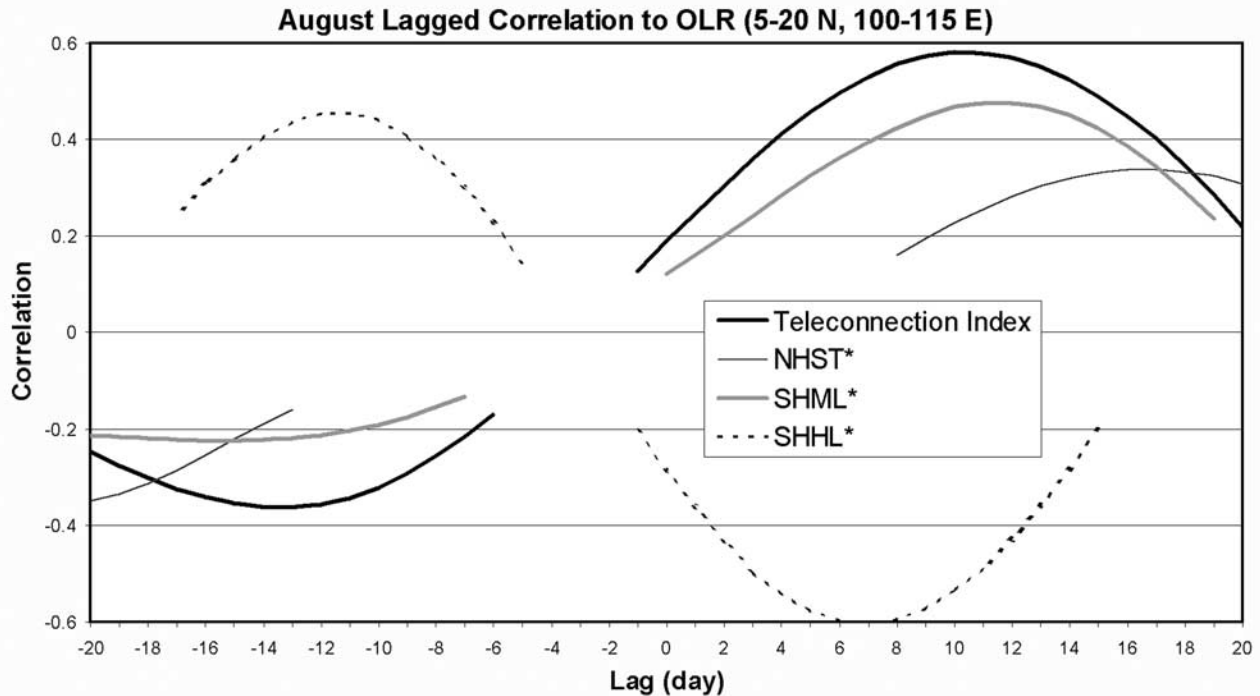


Figure 12. August lagged correlation of OLR in the sector 5–20°N, 100–115°E for anomaly sea level pressures including SHHL* at 65°S, 145°E, SHML* at 40°S, 150°E, and NHST* at 25°N, 125°E. Positive lags indicate that OLR leads the pressure anomaly. Data are filtered to periods of 25–75 days. All correlations shown are statistically significant at 95% confidence.

the annual cycle and synoptic-scale variations are removed from the geopotential fields while intraseasonal variations are retained. Figure 13 includes a wider range of frequencies than in Figure 12 to display a more complete development of the pattern. No temporal offsets are applied for cycles comprising the composite as clear offsets were not found between the cases.

[47] Of the six stages shown in Figure 13, the first panel (Figure 13a) displays the composite for 14 July before the teleconnection anomalies are seen to form. A high centered near 60°S, 125°E extends northwestward over the Indian Ocean with a low to the west centered at 55°S, 55°E. There are a chain of anomalies across the SH high and middle latitudes. The SH wave number one pattern (not shown) includes a ridge over the Indian Ocean at 40°S during the middle of July. By 22 July, the high seen in Figure 13a has split into two components. One component is centered near 60°E, and the other is centered near 140°E (Figure 13b). A low has moved between the two highs. On 30 July, shortly before the period of rapid intensification, the high-low-high pattern seen in Figure 13b has migrated eastward with the western high now weakened and centered near 105°E (Figure 13c). The low has also slightly weakened and is centered south of Australia near 125°E. The eastern high has intensified and is now south of New Zealand. Also by 30 July, a lower-tropospheric high is beginning to develop in the NH subtropical region over the extreme western Pacific Ocean.

[48] Figure 13 indicates that the longitudes near western Australia are favorable for development of two of the teleconnection anomalies. By 5 August, the familiar three

cell pattern across the equator is apparent, and the SH anomalies have rapidly intensified (Figure 13d). The western high has moved slightly east to near 130°E and has reached an intensity of 64.1 geopotential meters (gpm). The low has moved south and has reached a center intensity of 56.1 gpm. The wave number 1 pattern for this time includes a midlatitude ridge over Australia. The NH subtropical cell is centered offshore near 155°E and is weaker than the main SH anomalies as its amplitude is 15.9 gpm. The eastern high of the former high-low-high pattern in the SH has become the greatly weakened feature just east of New Zealand.

[49] The 15 August is about the time of maximum intensity for the teleconnection anomalies (Figure 13e). The eastern high of the high-low-high pattern seen previously in the SH has disappeared by 15 August, while another high has intensified near the Antarctic Peninsula. The low and the remaining high of the former high-low-high pattern have intensified and their centers have moved eastward of Australia. The high is now centered near New Zealand with an intensity of 75.2 gpm, and the low is to the south with a center intensity of 85.5 gpm. In the NHST, the extreme western Pacific anomaly has moved slightly west to near 135°E. The teleconnection anomalies slowly weaken after mid-August.

[50] By 29 August, the SH anomalies have weakened and stretched longitudinally (Figure 13f). The NH subtropical anomaly has also weakened. There is a lower frequency response in the SH that lingers after the three primary teleconnection anomalies weaken. Figure 13f shows a pattern with resemblance to the high latitude mode, as geopotential height is reduced at high latitudes and increased at

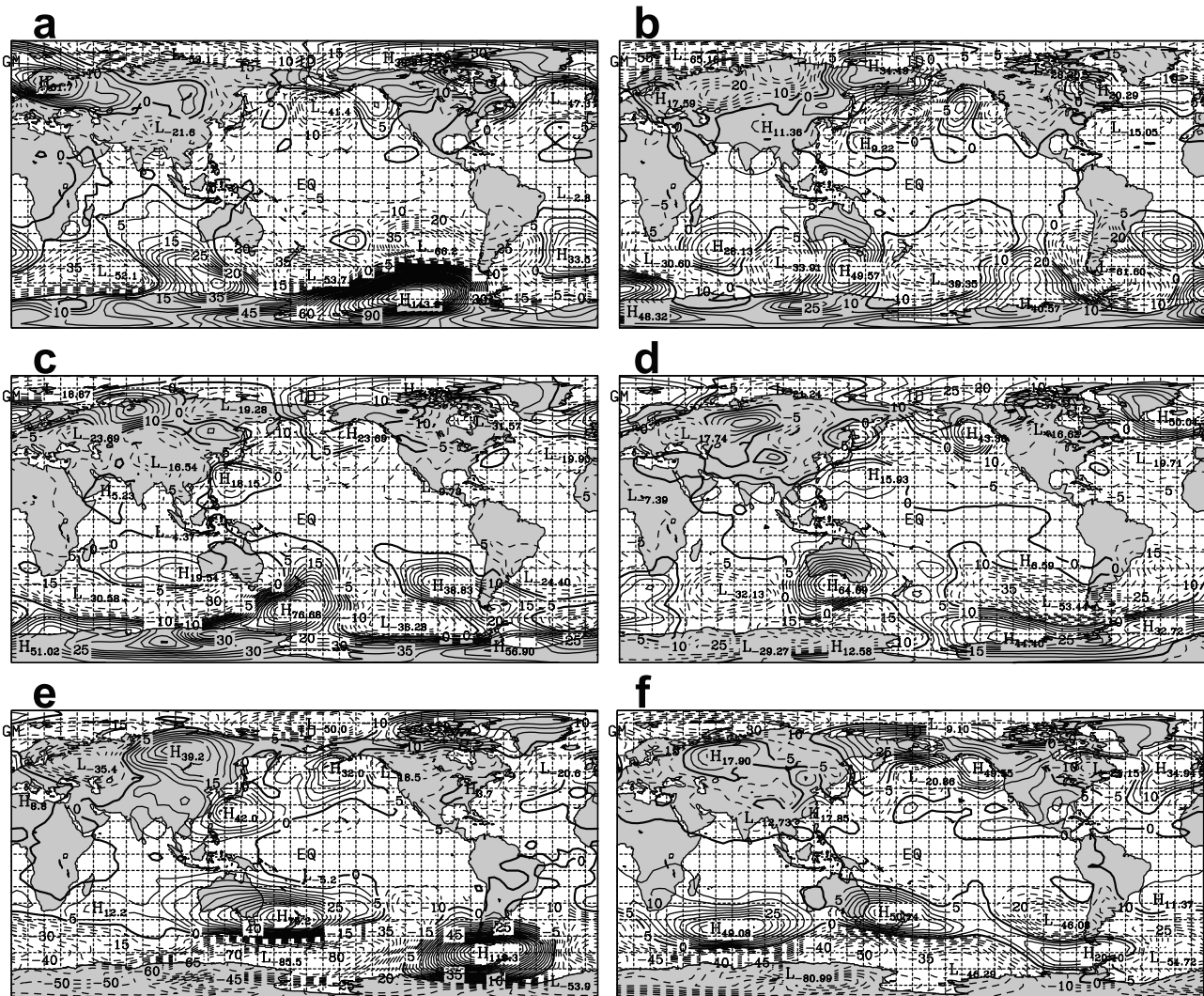


Figure 13. Daily composite difference in geopotential height (gpm) at 850 hPa between 5 positive phase teleconnection anomaly years and the 1977–1999 mean filtered to periods of 15 days or longer. (a) 14 July, (b) 24 July, (c) 30 July, (d) 5 August, (e) 15 August, and (f) 29 August. Contour interval is 5 m. Thick contour is 0.

middle latitudes. This lingering SH pattern is especially captured by lower frequencies, suggesting an interaction between the intraseasonal timescales and slightly lower frequencies. During the development of the anomalies, there has been a gradual eastward movement of the centers of the principal SH anomalies. The wave number 1 pattern migrates eastward consistent with the changes. In summary, there appears to be a strong longitudinal preference for the rapid growth of the SH teleconnection anomalies, with development favored for anomalies moving into the region near 110°E. The development of the negative phase of the teleconnection (not shown) is similar to that of the positive phase, except that the sign of the anomalies are reversed.

[51] Figure 14 shows the composite OLR averaged for 16 July to 15 August. The 1977–1997 daily mean is subtracted from the OLR, which is then filtered to intraseasonal variations with periods of 30–75 days. A time average is shown to emphasize the influence of lower frequency oscillations within the 30–75-day range on the OLR field

near Indonesia. Figure 14 helps show how tropical convection and the SH pressure anomalies are linked. For both the positive and negative phases of the teleconnection, an OLR anomaly near Indonesia is located between the NH subtropical component and the SH midlatitude component. The OLR anomaly is positive (reduced convection) for the positive teleconnection index Augusts and negative for negative index Augusts. For positive index Augusts, there is a negative OLR anomaly centered near 20°N, 120°E that is consistent with the increased precipitation over China seen in Figure 5. This negative OLR anomaly is generally west of the region of the increased surface pressure offshore (see Figure 2). Consequently, the anomalous geostrophic wind in the lower troposphere is northward, increasing the seasonal monsoon flow of warm, moist air toward the negative OLR anomaly (increased convection). In contrast, to the east of the increased subtropical surface pressure, where the anomalous geostrophic wind is southward, there is a positive OLR anomaly centered near 20°N, 155°E. The opposite phase of the OLR anomalies can be seen near the box in Figure 14b

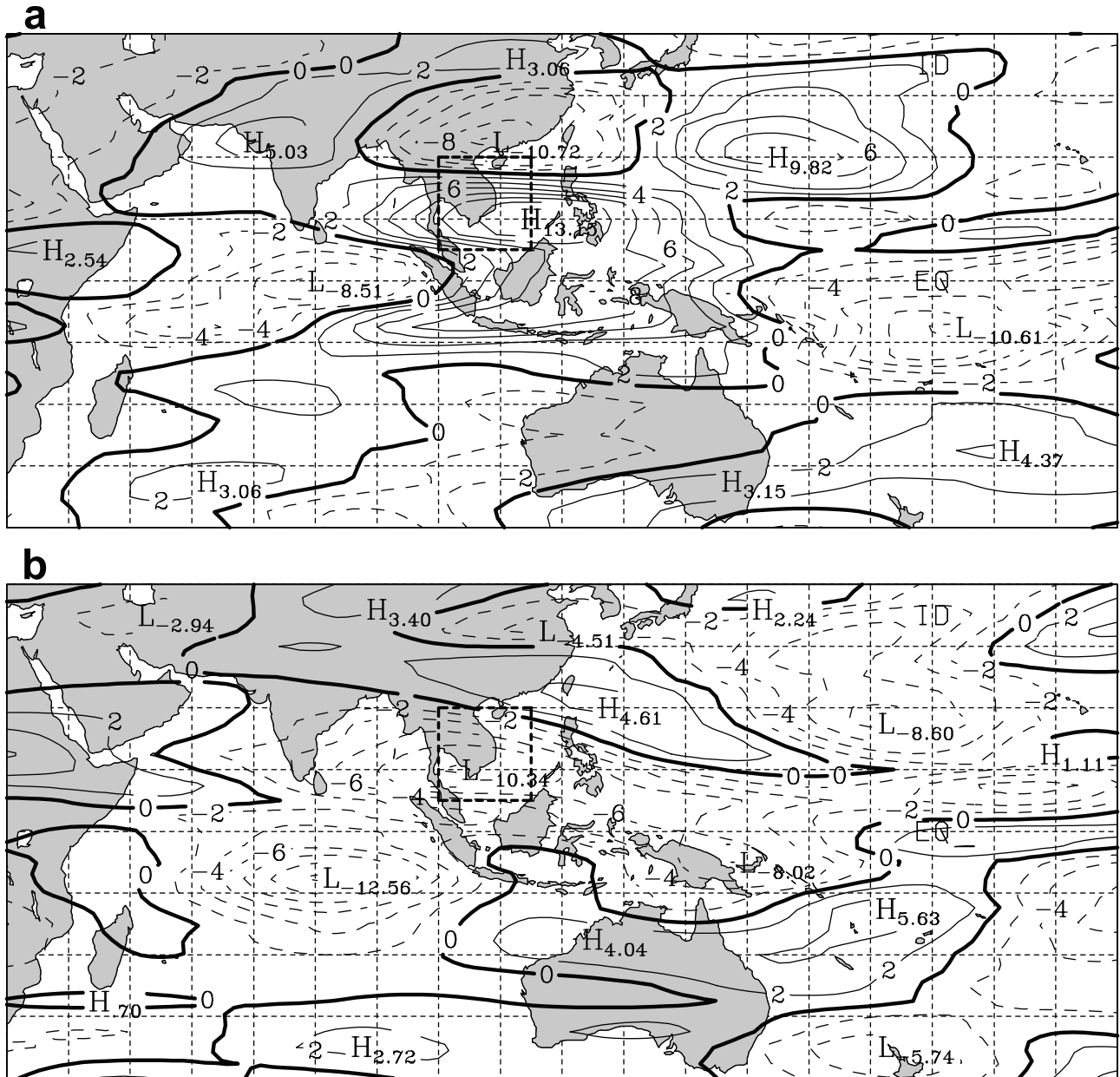


Figure 14. OLR (W m^{-2}) averaged for 16 July to 15 August. The OLR has been filtered to periods of 30–75 days and is displayed in composites of (a) five positive phase and (b) five negative phase teleconnection events. Contour interval is 2 W m^{-2} . The OLR inside the dashed line box is correlated to the teleconnection.

for negative index Augusts. On the other hand, while a negative anomaly indicating increased convection over the Equatorial Indian Ocean is seen in Figure 14a, there is no analogous positive feature in Figure 14b.

[52] Linkage between the tropical convection and the SH extratropics is also seen in Figure 15. Horizontal velocities are divided into divergent and rotation components for each of the teleconnection composites. Divergent wind components are then filtered to periods of 25–75 days. In Figure 15, the arrows display the filtered divergent velocity component at 850 and 300 hPa for 7 August, while the contours display the unfiltered wind speed at 300 hPa. The latter field shows the location of the subtropical and polar front jet streams in the upper troposphere. The 7 August

fields are representative of the growing stage of the teleconnection. The maximum in the SH subtropical jet stream begins over the Indian Ocean and extends over Australia. The subtropical jet is faster during the negative phase and weakened during the positive phase of the teleconnection.

[53] The vectors in Figure 15 show that the divergent circulation is active in the region of the subtropical jets near northern Australia. For the positive phase of the teleconnection, the anomalous divergent circulation represents an enhanced local Hadley cell with outward flow to the southwest at low levels from the tropical OLR anomalies near Indonesia (Figure 15c). At high levels (Figure 15a), the divergent flow from the SH subtropical jet is north and northeastward into the tropical OLR anomalies. The oppo-

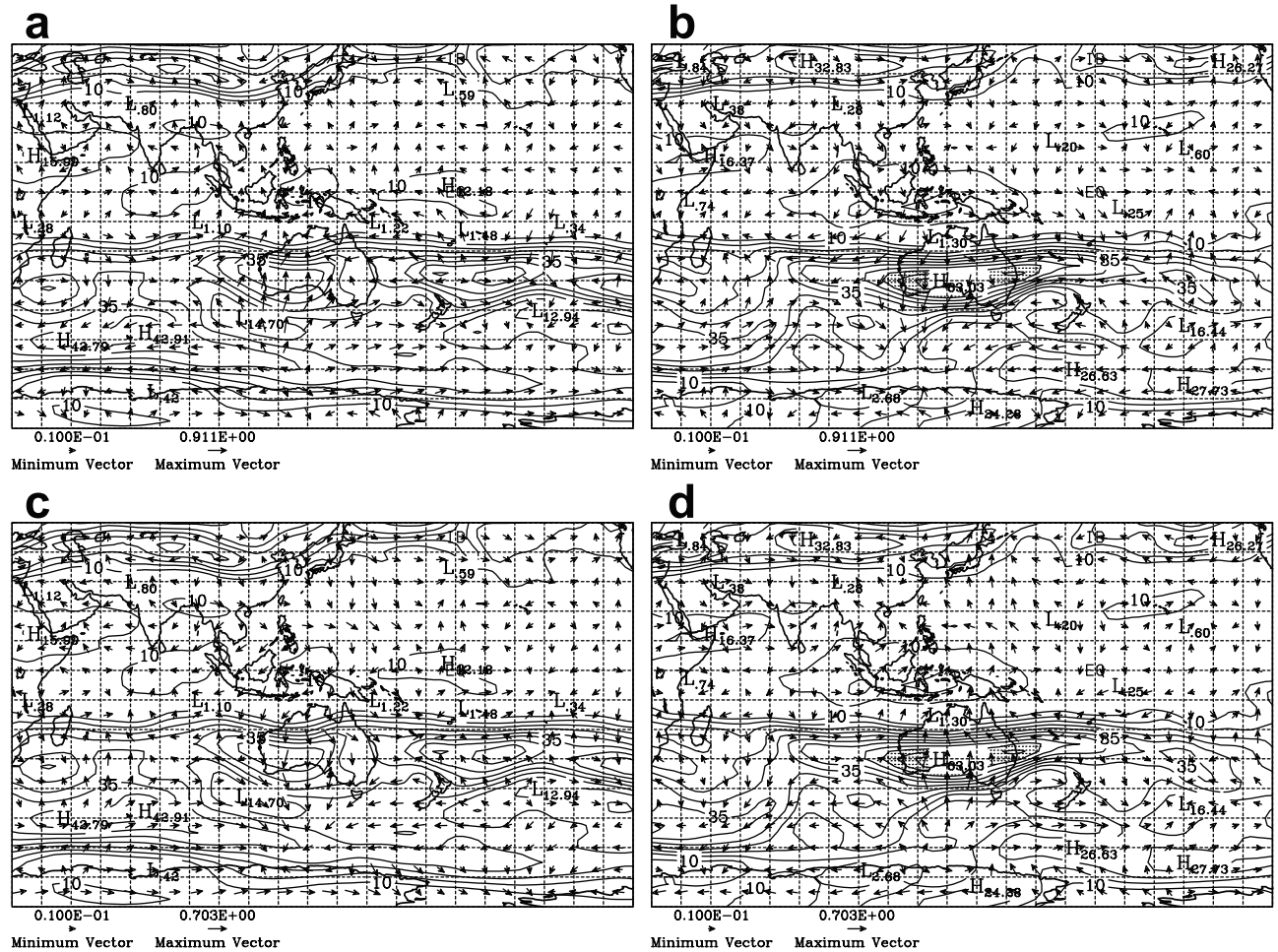


Figure 15. Divergent wind component (arrows, m s^{-1}) filtered to periods of 25–75 days for 7 August at (a) 300 hPa for the composite of five positive phase events, (b) 300 hPa for the composite of five negative phase events, (c) 850 hPa for the composite of five positive phase events, (d) 850 hPa for the composite of five negative phase events. The contours show the 300 hPa unfiltered wind speed. Contour interval is 5 m s^{-1} .

site is true for the negative phase. Previous studies have shown that enhanced tropical convection and variations in the SH subtropical jet streams are linked on intraseasonal timescales [e.g., *Hurrell and Vincent, 1991; Ko and Vincent, 1996*]. Figure 15 is consistent with those findings as the Coriolis torque to the left of the divergent wind is enhancing the SH subtropical jet stream at 300 hPa during negative index years. Furthermore, the divergent meridional circulation is seen to extend from the tropics to the latitude of the polar front jet near 50°S . The polar front jet tends to be intensified when the subtropical jet is weak. This can be seen in the contours of Figures 15a and 15b. The variations of the polar front jet typically have a reflection in the surface pressure pattern. This correspondence is seen between the pressure field of Figure 2 and the wind field of Figure 6. Also, the unbalanced development between hemispheres seen in Figure 13 is reflected in the divergent circulation in Figure 15. The NH circulation is less clearly ordered and there are multiple OLR anomalies there in Figure 14. Thus, through the divergent circulation at intraseasonal timescales, the teleconnection encompasses the SH split jet stream which can be seen in Figure 6. We have also

seen that the SH subtropical jet stream is well connected to tropical convection. Other key teleconnection linkages are to precipitation for the East Asian monsoon and elsewhere (Figure 5). Additional linkages in the Pacific sector are indicated by Figures 1 and 2.

[54] The preference for the teleconnection to be seen during late boreal summer may be related to the annual cycle of its intraseasonal components. *Kemball-Cook and Wang [2001]* show important differences in tropical intraseasonal behavior between May–June and August–October. For instance, they note that there is weaker eastward propagation and strong northwestward propagation in the western Pacific during August–October, unlike that for May–June. It is possible, therefore, that favorable tropical intraseasonal linkage involving the NH and SH components of the teleconnection is only present during a small portion of the annual cycle. Fine-tuned seasonal phase-locking has previously been found for the monsoon precipitation over China [*Samel et al., 1999*]. The boreal summer movement of the North Pacific Subtropical High [e.g., *Lu, 2001*] may also have a role in the limited seasonal duration of the teleconnection.

6. Conclusions

[55] Analyses of observed fields on both sides of the Equator reveal an intriguing teleconnection that links the late austral winter/boreal summer variability especially during August. Evaluation of the intraseasonal development of the teleconnection indicates that tropical convection on that timescale provides the forcing. Numerical simulations with the NCAR CCM2 produce a teleconnection that appears surprisingly similar to that observed and occurs about the same time of year. Thus, numerical simulations may be a tool for studying the teleconnection. Dissimilar to the observed feature, however, the forcing for the CCM2 simulations is in high southern latitudes.

[56] The observed teleconnection includes three primary anomalies in the surface pressure field for the West Pacific sector: (1) a SHHL component near Wilkes Land, Antarctica and the Ross Sea area, (2) a SH midlatitude component near Australia and New Zealand, and (3) a NH subtropical component over the extreme western Pacific Ocean. The monthly average surface pressure for the SH midlatitude anomaly is negatively correlated to the SH high-latitude anomaly. There is also a positive interhemispheric correlation in surface pressure between the SH midlatitude anomaly and the NH subtropical anomaly. An index to measure the phase and intensity has been defined based on the three primary anomalies. These anomalies develop on intraseasonal timescales and have a lagged correlation to tropical convection near Indonesia.

[57] The teleconnection links regions of highly important climate variability. Impacted features are the Antarctic circumpolar trough, the split jet in the SH, and the East Asian monsoon in the NH. Furthermore, the teleconnection also encompasses correlations to the surface pressure near the Aleutian Islands in high northern latitudes. Thus the teleconnection influences the Pacific basin from the Antarctic to the Arctic basin. The important consequences include modulation of the East Asian monsoon, as local precipitation is significantly increased during Augusts of increased pressure over Australia. Precipitation is also significantly impacted at locations in the tropics and SH middle latitudes. In summary, the West Pacific sector appears to be a crucial region for communication between high latitudes and low latitudes during late austral winter/boreal summer.

[58] **Acknowledgments.** We thank Dan Lubin for selecting the cloud modifications to CCM2. Biao Chen, Linjuan Gong, and Ying Sang assisted with the numerical simulations. This research was supported by NASA via grants NAG5-7750 and NAGW-2718 and by NSF via grant ATM-9820042. The computations were performed with project 36091005 on the CRAY Y-MP of NCAR, which is supported by NSF, and on the CRAY Y-MP of the Ohio Supercomputer Center (OSC), which is supported by the State of Ohio. This is contribution 1247 of the Byrd Polar Research Center. We thank Charles Bender for grant PAS689 from the OSC Director's Discretionary Fund.

References

- Bretherton, C. S., M. Widmann, V. P. Dymnikov, J. M. Wallace, and I. Blade, The effective number of spatial degrees of freedom of a time-varying field, *J. Clim.*, **12**, 1990–2009, 1999.
- Bromwich, D. H., B. Chen, and K. M. Hines, Global atmospheric impacts induced by year-round open water adjacent to Antarctica, *J. Geophys. Res.*, **103**, 11,173–11,189, 1998a.
- Bromwich, D. H., B. Chen, K. M. Hines, and R. I. Cullather, Global atmospheric responses to Antarctic forcing, *Ann. Glaciol.*, **27**, 521–527, 1998b.
- Bromwich, D. H., A. N. Rogers, P. Källberg, R. I. Cullather, J. W. C. White, and K. J. Kreutz, ECMWF analyses and reanalyses depiction of ENSO signal in Antarctic precipitation, *J. Clim.*, **13**, 1406–1420, 2000.
- Chen, B., S. R. Smith, and D. H. Bromwich, Evolution of the tropospheric split jet over the south Pacific Ocean during the 1986–1989 ENSO cycle, *Mon. Weather Rev.*, **124**, 1711–1731, 1996.
- Cullather, R. I., D. H. Bromwich, and M. L. Van Noert, Interannual variations in Antarctic precipitation related to El Niño–Southern Oscillation, *J. Geophys. Res.*, **101**, 19,109–19,118, 1996.
- Davidson, N. E., J. L. McBride, and B. J. McAvaney, The onset of the Australian monsoon during winter MONEX: Synoptic aspects, *Mon. Weather Rev.*, **111**, 496–516, 1983.
- Domrös, M., and G. Peng, *The Climate of China*, 351 pp., Springer-Verlag, New York, 1988.
- Ebert, E. E., and J. A. Curry, A parameterization of ice cloud optical properties for climate models, *J. Geophys. Res.*, **97**, 3831–3836, 1992.
- Fan, Z., and R. J. Oglesby, A 100-yr CCM1 simulation of North China's hydrologic cycle, *J. Clim.*, **9**, 189–204, 1996.
- Frederiksen, C. S., D. P. Rowell, R. C. Balgovind, and C. K. Folland, Multidecadal simulations of Australian rainfall variability: The role of SSTs, *J. Clim.*, **12**, 357–379, 1999.
- Gloersen, P., Modulation of hemispheric sea-ice cover by ENSO events, *Nature*, **373**, 503–506, 1995.
- Hack, J. J., B. A. Boville, B. P. Briegleb, J. T. Kiehl, P. J. Rasch, and D. L. Williamson, Description of the NCAR Community Climate Model (CCM2), *NCAR Tech. Note, NCAR/TN-382+STR*, Natl. Cent. for Atmos. Res., Boulder, Colo., 1993.
- Hack, J. J., B. A. Boville, J. T. Kiehl, P. J. Rasch, and D. L. Williamson, Climate statistics from the National Center for Atmospheric Research community climate model CCM2, *J. Geophys. Res.*, **99**, 20,785–20,813, 1994.
- Hendon, H. H., and M. L. Salby, The life cycle of the Madden–Julian Oscillation, *J. Atmos. Sci.*, **51**, 2225–2237, 1994.
- Hines, K. M., D. H. Bromwich, and G. J. Marshall, Artificial surface pressure trends in the NCEP/NCAR Reanalysis over the Southern Ocean and Antarctica, *J. Clim.*, **13**, 3940–3952, 2000.
- Horel, J. D., and J. M. Wallace, Planetary scale atmospheric phenomena associated with the Southern Oscillation, *Mon. Weather Rev.*, **109**, 813–823, 1981.
- Hurrell, J. W., and D. G. Vincent, On the maintenance of short-term subtropical wind maxima in the Southern Hemisphere during SOP-1, *FGGE, J. Clim.*, **4**, 1009–1022, 1991.
- Joseph, P. V., B. Liebmann, and H. H. Hendon, Interannual variability of the Australian summer monsoon onset: Possible influence of Indian summer monsoon and El Niño, *J. Clim.*, **4**, 529–538, 1991.
- Kalnay, E., et al., The NCEP/NCAR 40-year reanalysis project, *Bull. Am. Meteorol. Soc.*, **77**, 437–471, 1996.
- Kemball-Cook, S., and B. Wang, Equatorial waves and air–sea interaction in the boreal summer intraseasonal oscillation, *J. Clim.*, **14**, 2923–2942, 2001.
- Kiehl, J. T., Sensitivity of a GCM climate simulation to differences in continental versus maritime cloud drop size, *J. Geophys. Res.*, **99**, 23,107–23,115, 1994.
- Kiladis, G. N., and K. C. Mo, Interannual and intraseasonal variability in the Southern Hemisphere, in *Meteorology of the Southern Hemisphere*, edited by D. J. Karoly and D. G. Vincent, pp. 307–336, Am. Meteorol. Soc., Boston, Mass., 1998.
- Kiladis, G. N., and K. M. Weickmann, Circulation anomalies associated with tropical convection during northern winter, *Mon. Weather Rev.*, **120**, 1900–1923, 1992.
- Kistler, R., et al., The NCEP/NCAR 50-year reanalysis, *Bull. Am. Meteorol. Soc.*, **82**, 247–267, 2001.
- Ko, K.-C., and D. G. Vincent, Behavior of one- to two-week summertime subtropical wind maxima over the South Pacific during an ENSO cycle, *J. Clim.*, **9**, 5–16, 1996.
- Krishnamurti, T. N., P. K. Jayakumar, J. Sheng, N. Surgi, and A. Kumar, Divergent circulations on the 30 to 50 day time scale, *J. Atmos. Sci.*, **42**, 364–375, 1985.
- Lau, K.-M., and M. T. Li, The monsoon of east Asia and its global association: A survey, *Bull. Am. Meteorol. Soc.*, **65**, 114–125, 1984.
- Lau, K. M., and P. H. Chan, Aspects of the 40–50 day oscillation during the northern summer as inferred from outgoing longwave radiation, *Mon. Weather Rev.*, **114**, 1354–1367, 1986.
- Lau, K.-M., and S. Yang, Seasonal variation, abrupt transition, intraseasonal variability associated with the Asian summer monsoon in the GLA GCM, *J. Clim.*, **9**, 965–985, 1996.
- Lau, K.-M., G. J. Yang, and S. H. Shen, Seasonal and intraseasonal clima-

- tology of summer monsoon rainfall over East Asia, *Mon. Weather Rev.*, **116**, 18–37, 1988.
- Lau, K.-M., P.-J. Sheu, and I.-S. Kang, Multiscale low-frequency circulation modes in the global atmosphere, *J. Atmos. Sci.*, **51**, 1169–1193, 1994.
- Lu, R., Interannual variability of the summertime North Pacific Subtropical High and its relation to atmospheric convection over the warm pool, *J. Meteorol. Soc. Jpn.*, **79**, 771–783, 2001.
- Lubin, D., B. Chen, D. H. Bromwich, R. C. J. Summerville, W.-H. Lee, and K. M. Hines, The impact of Antarctic cloud radiative properties on a GCM climate simulation, *J. Clim.*, **11**, 447–462, 1998.
- Madden, R. A., and P. R. Julian, Detection of a 40–50-day oscillation in the zonal wind in the tropical Pacific, *J. Atmos. Sci.*, **28**, 702–708, 1971.
- Madden, R. A., and P. R. Julian, Observations of the 40–50-day tropical oscillation: A review, *Mon. Weather Rev.*, **121**, 814–837, 1994.
- Maloney, E. D., and D. L. Hartmann, Frictional moisture convergence in a composite life cycle of the Madden–Julian Oscillation, *J. Clim.*, **11**, 2387–2403, 1998.
- Maloney, E. D., and D. L. Hartmann, The sensitivity of intraseasonal variability in the NCAR CCM3 to changes in convective parameterization, *J. Clim.*, **14**, 2015–2034, 2001.
- Mo, K. C., and R. W. Higgins, The Pacific–South America modes and tropical convection during the Southern Hemisphere winter, *Mon. Weather Rev.*, **126**, 1581–1596, 1998.
- Park, C. K., and S. D. Schubert, On the nature of the 1994 East Asian summer drought, *J. Clim.*, **10**, 1056–1070, 1997.
- Rogers, J. C., and H. van Loon, Spatial variability of sea level pressure and 500 hPa height anomalies over the Southern Hemisphere, *Mon. Weather Rev.*, **110**, 1373–1392, 1982.
- Salby, M. L., and H. H. Hendon, Intraseasonal behavior of clouds, temperature, and motion in the tropics, *J. Atmos. Sci.*, **51**, 2207–2224, 1994.
- Samel, A. N., W.-C. Wang, and X.-Z. Liang, The monsoon rainband over China and relationships with the Eurasian circulation, *J. Clim.*, **12**, 115–131, 1999.
- Sardeshmukh, P. D., and B. J. Hoskins, The generation of global rotational flow by steady idealized tropical divergence, *J. Atmos. Sci.*, **45**, 1228–1251, 1988.
- Simmonds, I., and W. F. Budd, Sensitivity of the southern hemisphere circulation to leads in the Antarctic pack ice, *Q. J. R. Meteorol. Soc.*, **117**, 1003–1024, 1991.
- Simmonds, I., and T. H. Jacka, Relationships between the interannual variability of Antarctic sea ice and the Southern Oscillation, *J. Clim.*, **8**, 637–647, 1995.
- Slingo, J. M., et al., Intraseasonal oscillations in 15 atmospheric general circulation models: Results from an AMIP diagnostic subproject, *Clim. Dyn.*, **12**, 325–357, 1996.
- Smith, S. R., and C. R. Stearns, Antarctic pressure and temperature anomalies surrounding the minimum in the Southern Oscillation index, *J. Geophys. Res.*, **98**, 13,071–13,083, 1993.
- Thompson, D. W. J., and J. M. Wallace, Annular modes in the extratropical circulation, part I, Month-to-month variability, *J. Clim.*, **13**, 1000–1016, 2000.
- Trenberth, K. E., G. W. Branstator, D. Karoly, A. Kumar, N.-C. Lau, and C. Ropelewski, Progress during TOGA in understanding and modeling global teleconnections associated with tropical sea surface temperatures, *J. Geophys. Res.*, **103**, 14,291–14,324, 1998.
- Tyrrell, G. C., D. J. Karoly, and J. L. McBride, Links between tropical convection and variations of the extratropical circulation during TOGA COARE, *J. Atmos. Sci.*, **53**, 2735–2748, 1996.
- Tzeng, R.-Y., D. H. Bromwich, T. R. Parish, and B. Chen, NCAR CCM2 simulation of the modern Antarctic climate, *J. Geophys. Res.*, **99**, 23,131–23,148, 1994.
- Vincent, D. G., T. Sperling, A. Fink, S. Zube, and P. Speth, Intraseasonal oscillation of convection activity in the tropical Southern Hemisphere: May 1984–April 1986, *J. Clim.*, **4**, 40–53, 1991.
- Vose, R. S., R. L. Schmoyer, P. M. Steurer, T. C. Peterson, R. Heim, T. R. Karl, and J. K. Eischeid, The Global Historical Climatology Network: Long-term monthly temperature, precipitation, sea level pressure, and station pressure data, *NDP-041*, Carbon Dioxide Inf. Anal. Cent., Oak Ridge Natl. Lab., Oak Ridge, Tenn., 1992.
- Waliser, D. E., C. Jones, J.-K. E. Schemm, and N. E. Graham, A statistical extended-range tropical forecast model based on the slow evolution of the Madden–Julian Oscillation, *J. Clim.*, **12**, 1918–1939, 1999.
- Wang, W.-C., and K. Li, Precipitation fluctuation over semiarid region in northern China and the relationship with El Niño/Southern Oscillation, *J. Clim.*, **3**, 769–783, 1990.
- Wang, B., and H. Rui, Synoptic climatology of transient tropical intraseasonal convection anomalies, *Meteorol. Atmos. Phys.*, **44**, 43–61, 1990.
- Wang, W., and M. E. Schlesinger, The dependence on convection parameterization of the tropical intraseasonal oscillation simulated by the UIUC 11-layer atmospheric GCM, *J. Clim.*, **12**, 1423–1457, 1999.
- Wang, B., and X. Xie, Coupled modes of the warm pool climate system, part I, The role of air–sea interaction in maintaining Madden–Julian Oscillation, *J. Clim.*, **11**, 2116–2135, 1998.
- Wang, B., and X. Xu, Northern Hemisphere summer monsoon singularities and climatological intraseasonal oscillation, *J. Clim.*, **10**, 1071–1085, 1997.
- Weickmann, K. M., G. R. Lussky, and J. E. Kutzbach, Intraseasonal fluctuations of outgoing longwave radiation and 250 mb streamfunction during northern winter, *Mon. Weather Rev.*, **113**, 941–961, 1985.
- Xie, P., and P. A. Arkin, Global precipitation: A 17-year monthly analysis based on gauge observations, satellite estimates and numerical model outputs, *Bull. Am. Meteorol. Soc.*, **78**, 2539–2558, 1997.
- Zhu, B., and B. Wang, The 30–60 day convection seesaw between the tropical Indian and western Pacific Oceans, *J. Atmos. Sci.*, **50**, 184–199, 1993.

K. M. Hines, Polar Meteorology Group, Byrd Polar Research Center, The Ohio State University, 108 Scot Hall, 1090 Carmack Road, Columbus, OH 43210-1002, USA. (hines.91@osu.edu)

D. H. Bromwich, Atmospheric Sciences Program, Department of Geography, The Ohio State University, Columbus, OH, USA.